

STRUCTURE AND DYNAMICS OF CORONAL PLASMAS

NASA Grant NAGW-4081

1N-92
394383

Final Report

For the Period 1 July 1994 through 30 June 1998

Principal Investigator
Dr. Leon Golub

October 1998

Prepared for:

National Aeronautics and Space Administration
Washington, D.C.

Smithsonian Institution
Astrophysical Observatory
Cambridge, Massachusetts 02138

The Smithsonian Astrophysical Observatory
is a member of the
Harvard-Smithsonian Center for Astrophysics

The NASA Technical Officer for this grant is William J. Wagner, Code: SSS, National Aeronautics and Space Administration Headquarters, Washington, D.C. 20546.



Work Completed Under This Grant:

The following is a brief summary of the published papers which have been supported by Grant NAGW-4081 within the present grant performance period.

1. The paper "Coronal Structures Observed in X-rays and H α Structures" was published in the Kofu Symposium proceedings. The study analyzes cool and hot behavior of two x-ray events, a small flare and a surge. We find that a large H α surge appears in x-rays as a very weak event, while a weak H α feature corresponds to the brightest x-ray emission on the disk at the time of the observation. Calculations of the heating necessary to produce these signatures, and implications for the driving and heating mechanisms of flares vs. surges are presented.

A copy of the paper is appended to this report.

2. The paper "Differential Magnetic Field Shear in an Active Region" has been published in The Astrophysical Journal. We have compared the 3D extrapolation of magnetic fields with the observed coronal structure in an active region. Based on the fit between observed coronal structure throughout the volume of the region and the calculated magnetic field configurations, we propose a differential magnetic field shear model for this active region. The decreasing field shear in the outer portions of the AR may indicate a continual relaxation of the magnetic field with time, corresponding to a net transport of helicity outward.

A copy of the paper is appended to this report.

3. The paper "Difficulties in Observing Coronal Structure" has been published in the journal Solar Physics. In this paper we discuss the evidence that the temperature and density structure of the corona are far more complicated than had previously been thought. The discussion is based on five studies carried out by our group on coronal plasma properties, showing that any one x-ray instrument does not see all of the plasma present in the corona, that hot and cool material may appear to be co-spatial at a given location in the corona, and that simple magnetic field extrapolations provide only a poor fit to the observed structure.

A copy of the paper is appended to this report.

4. The paper "Analysis and Comparison of Loop Structures Imaged with NIXT and Yohkoh/SXT" has been published in Astronomy and Astrophysics. In this paper we analyze and compare a variety of coronal loops, deriving loop pressure and emission measure from loop models. We are able to determine the volume filling factor in the corona, which is found to be in the range 0.001 - 0.01 for compact loops, and of order 1 for large structures. The small values suggest highly filamented structures, especially at lower temperatures.

A copy of the paper is appended to this report.

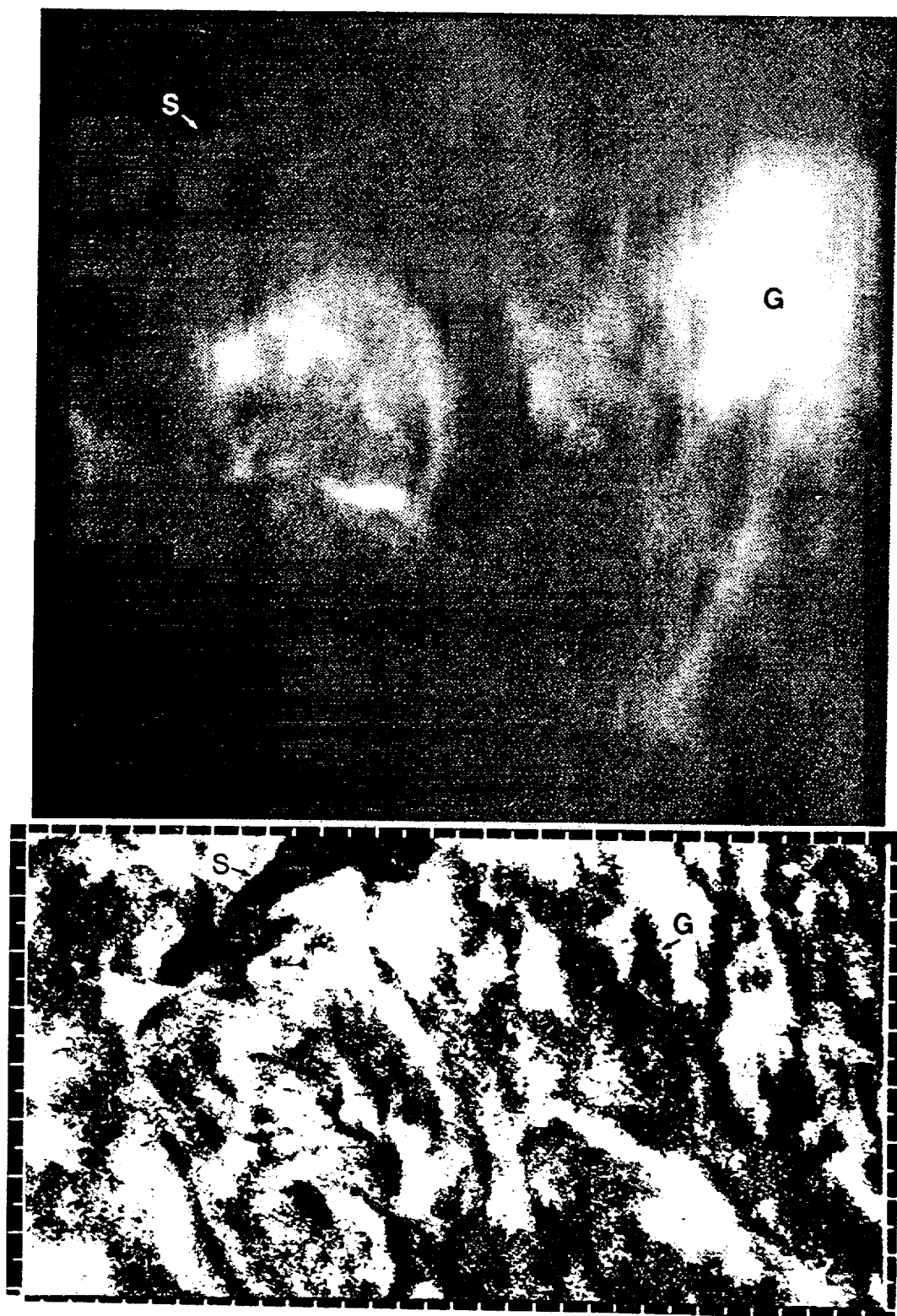


Fig. 2. Active region AR 6713 observed in X-ray with the NIXT and in H α with the MSDP (blue/red corresponds to blue/redshifts)

problem is discussed self-consistently in order to understand the mechanism which increases the pressure at the surge base (see for more details Schmieder *et al.* 1994b). The basic idea is that if the surge is pressure driven, then the driver gas is expected to be visible in X-rays.

Table 1 Coronal Parameters Measured by the NIXT Instrument.

T_e (10^6 K)	Relative Sensitiv.	Height (10^9 cm)	EI_{min} (10^{28} cm $^{-5}$)	EI @ C –	EI @ G –	n_e @ C (10^9 cm $^{-3}$)	n_e @ G –
3.00	1.	15	0.56	3.4	67	1.5	6.6
2.0	0.63	10	0.9	5.4	108	2.4	11
1.5	0.90	7.5	0.6	3.6	72	2.4	11
1.0	4.5	5	0.13	0.82	14	1.2	5.5

If this temperature is well below 10^6 K then the emission from the driver gas would be outside the sensitivity range of NIXT (Table 1). However, there are several arguments against such a low temperature. First, we note that the driving gas must have a temperature of at least 10^5 K in order to raise the plasma to the observed height if there is no injection of cool material from below. In addition, the radiative cooling time for plasma at that temperature is very short compared with the expansion time of the driver gas; consequently there would have to be continuous heating in order to maintain the driver temperature. A continuous heating, however, would inevitably drive the temperature to values well above 10^5 K.

Note that the emission intensity, EI , is strongly dependent on the filling factors . If they are of order unity then the emission measure would be easily observable by NIXT.

3. Conclusion

Hence, our observations rule out the pressure driven models with large filling factors. On the other hand, if the filling factors are of order 10%, then EI is reduced by 4 orders of magnitude, and would not be observable by NIXT. An important question, therefore, is how we can evaluate the filling factors.

References

1. Schmieder, B., Mein N., Golub, L., Davila, J.M., Brosius, J. Thomas, R., 1993, SOHO workshop, ESA SP 348, 257
2. Schmieder, B., Mouradian Z., Golub, L., Antiochos, S.K., 1994a, *Memorie del'Osserv. di Catania*
3. Schmieder, B., Golub, L., Antiochos, S.K., 1994b, *ApJ* in press

CORONAL STRUCTURES OBSERVED IN X-RAYS (NIXT) AND $H\alpha$ SURGES

B. Schmieder ¹, Z. Mouradian ¹, L. Golub ², S. Antiochos ³

¹ *Observatoire de Paris, Section Meudon, 92195 Meudon, France*

² *Harvard-Smithsonian Center, 60 Garden Street, Cambridge, MA 02138, U.S.A.*

³ *Naval Research Laboratory, Washington, DC 20375, U.S.A.*

Abstract

Ground-based coordinated observations with the Multichannel subtractive double pass spectrograph (MSDP) and the heliograph in Meudon allowed us to portray the chromospheric intensity and velocity fields below coronal structures observed with the Normal Incidence X-ray Telescope (NIXT). On July 11, 1991 (eclipse day) we have identified in AR 6713 (N38 W 42) the X-ray signatures of the network, subflares, filaments and surges. The largest $H\alpha$ surge has only weak emission in X-ray, while a weak $H\alpha$ feature corresponds to a very bright x-ray subflare. We calculate the emission measures of these events and give some constraints on the triggering mechanisms of surges.

1. Introduction and Observations

The observations have been described in details by Schmieder *et al.* (1993, 1994a,b). We shall report them briefly. A recurrent surge (S) has been observed with the Meudon heliograph (Fig. 1). The figure 2 displays the X-ray image observed by NIXT at 63.5 Å, sensitive at $T=1$ and 3×10^6 K in the top pannel and in the bottom pannel the $H\alpha$ image (composite of intensity and velocity) obtained with the MSDP operating at Meudon. The letter S indicates the large $H\alpha$ surge and the X-ray weak signature, the letter G the X-ray microflare and the $H\alpha$ weak intensity signature. Along the surge S and in G large $H\alpha$ flows are detected. The microflare G is directly related to a chromospheric dynamical event. This may be an exemple of dynamism without evident energy transport.

2. Model

The data set described above provides a unique opportunity to test models of surges and, in particular, models in which the motions are driven by gas pressure gradients. The

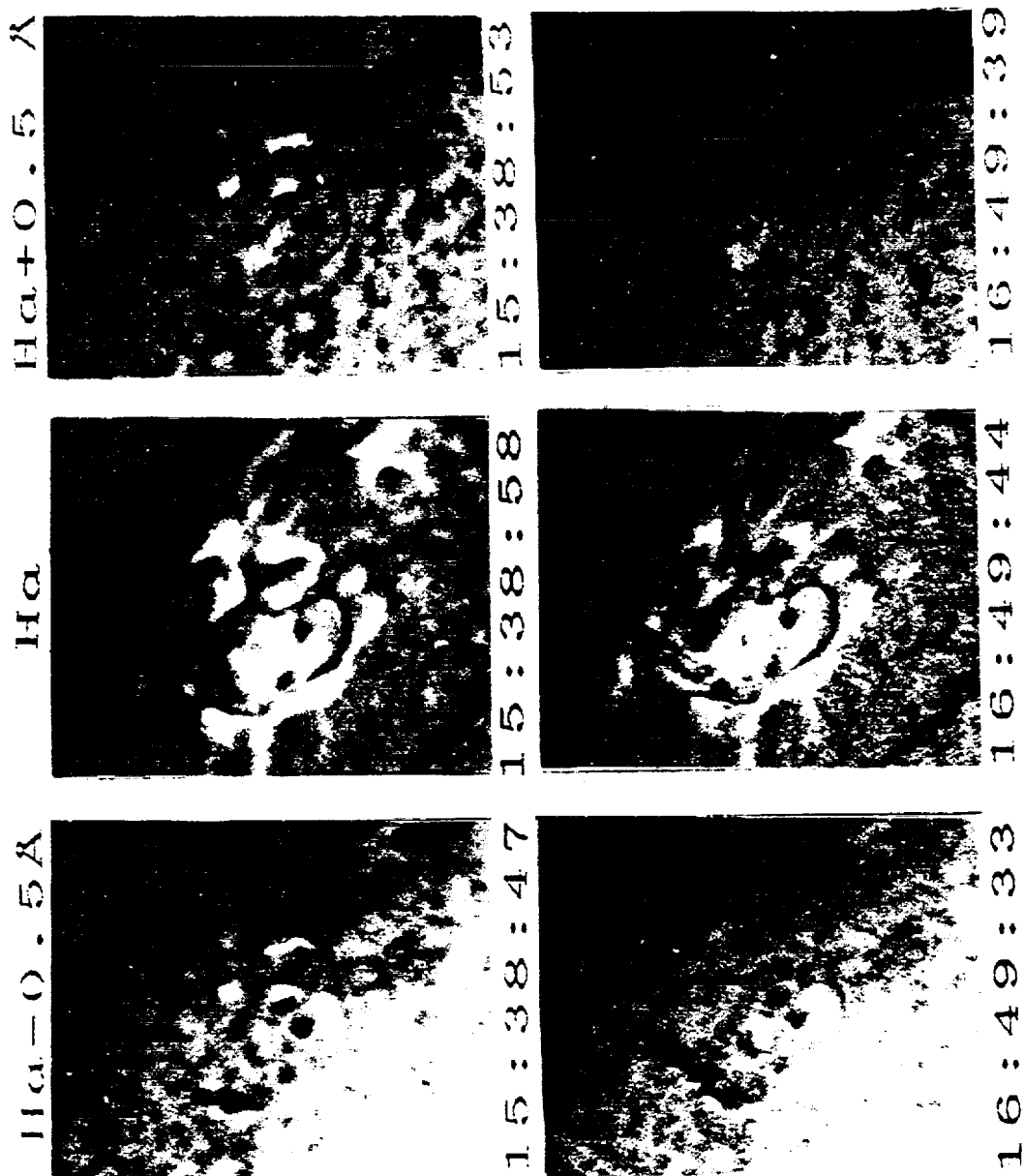


Fig. 1. Meudon 3- λ heliograms of AR 6713 on July 11, 1991

Fig. 1. Meudon 3- λ heliograms of AR 6713 on July 11, 1991

DIFFERENTIAL MAGNETIC FIELD SHEAR IN AN ACTIVE REGION

B. SCHMIEDER,¹ P. DÉMOULIN,¹ G. AULANIER,¹ AND L. GOLUB²

Received 1995 December 1; accepted 1996 March 7

ABSTRACT

The three-dimensional extrapolation of magnetic field lines from a magnetogram obtained at Kitt Peak allows us to understand the global structure of the NOAA active region 6718, as observed in X-rays with the Normal Incidence X-ray Telescope (NIXT) and in H α with the Multichannel Subtractive Double Pass spectrograph (MSDP) in Meudon on 1991 July 11. This active region was in a quiet stage. Bright X-ray loops connect plages having field strengths of ~ 300 G, while H α fibrils connect penumbrae having strong spot fields to the surrounding network. Small, intense X-ray features in the moat region around a large spot, which could be called X-ray-bright points, are due mainly to the emergence of magnetic flux and merging of these fields with surrounding ones. A set of large-scale, sheared X-ray loops is observed in the central part of the active region. Based on the fit between the observed coronal structure and the field configurations (and assuming a linear force-free field), we propose a *differential magnetic field shear* model for this active region. The decreasing shear in outer portions of the active region may indicate a continual relaxation of the magnetic field to a lower energy state in the progressively older portions of the AR.

Subject headings: MHD — Sun: faculae, plages — Sun: magnetic fields

1. INTRODUCTION

Because of the high conductivity of the coronal plasma along magnetic field lines, and because of the low β of the plasma, the structure in an active region is determined largely by the magnetic field. Observations of the magnetic field in the photosphere is commonly based on the splitting of lines due to the Zeeman effect. At the photospheric level, only the distribution of magnetic flux is measured, while the field topology (field line connectivity) is difficult to establish from the photospheric field measurements. Although some high-resolution microwave interferometry is beginning to be used to deduce the magnetic structure in the corona, it is still necessary to assume a model for both the coronal field and plasma. Alternatively, to infer the large-scale three-dimensional structure at heights above those at which the magnetograph measurements are made (> 1000 km) we can extrapolate the measured photospheric field (Alissandrakis 1981; Sakurai 1982; Hannakam, Gary, & Teuber 1984) using a variety of successively more elaborate methods. If any currents in the region are confined to heights at or below the photosphere, the field above is a potential field. If not, a force-free field configuration ($\mathbf{J} \times \mathbf{B} = 0$, $\nabla \times \mathbf{B} = \alpha \mathbf{B}$) is commonly assumed because of the low plasma β , corresponding to $\mathbf{J} \parallel \mathbf{B}$.

This theoretical assumption has recently received support from observations: Metcalf et al. (1995) show, by computation of the magnetic field from the Stokes parameters observed in the Na I line, that the photospheric field is not force free but that it becomes force free roughly 400 km above the photosphere in a quiet active region.

There have been only a limited number of attempts in recent years to carry out direct comparisons between high-resolution coronal observations and magnetic field extrapolations. Several attempts have been made to explain the

onset of flares by testing the nonpotentiality of the fields. Typically, B_z is compared with H α fibrils (Schmieder et al. 1990) or Ly α fibrils (Gary et al. 1987). For nonflaring regions, only a few attempts have been made. Poletto et al. (1975), and Sakurai & Uchida (1977) successfully modeled some connected active regions observed with *Skylab* by using potential extrapolations of photospheric fields, and Sams, Golub, & Weiss (1992) confirmed a general agreement by using NIXT observations. Recently, McClymont & Mikic (1994) used a three-dimensional magnetohydrodynamic (MHD) code to analyze a highly sheared region; they found that, in agreement with observations, the highly sheared loops should have a thickness variation along their lengths of only 10%–20%.

It is reasonable to ask whether we always need such a huge code and supercomputer resources to analyze the magnetic fields of active regions. Do less sophisticated methods of extrapolation, which are much faster and more economical, give some insight into the observations? In the present study, we use a linear force-free field extrapolation, discuss its limitations, and show that some significant insights can be gained in understanding the observation. In particular, we may ask how the observed coronal loops correspond to the extrapolated magnetic field lines under this hypothesis and why the connectivity of the X-ray-bright structures follows the topology which is observed.

For this study, we have available a set of high-resolution data sets of a “quiet” active region in H α obtained with the Meudon MSDP, in soft X-ray observed by NIXT, and magnetic data from Kitt Peak. We have compared extrapolated magnetic field lines above the AR 6718 on 1991 July 11 with cold and hot structures by using H α fibrils and filaments (MSDP) and X-ray loops (NIXT).

2. INSTRUMENTS

2.1. NIXT

The Normal Incidence X-ray Telescope (NIXT) was launched on a NASA sounding rocket 1991 July 11 at 17:25 UT, during a solar eclipse. The NIXT instrument observes

¹ Observatoire de Paris, Section de Meudon, URA 2080, 92195 Meudon, Cedex Principal, France.

² Smithsonian Astrophysical Observatory, Harvard-Smithsonian Center for Astrophysics, Cambridge, MA 02138.

the full disk with a resolution less than $1''$; it is described in detail by Spiller et al. (1991). The multilayer mirror has a passband of 1.4 \AA at 63.5 \AA corresponding to two coronal lines, one of Mg x and one of Fe xvi, formed at $T \sim 1 \times 10^6 \text{ K}$ and $3 \times 10^6 \text{ K}$, respectively. The brightening of Mg x occurs near loop footpoints and often coincides with bright chromospheric regions of higher magnetic field strength (network, plages) and of higher density (Peres, Reale, & Golub 1994; Golub, Zirin, & Wang 1994). The brightening is caused by the presence at the loop footpoint of $T \sim 10^6 \text{ K}$ material with sufficient emission measure to produce a visible brightening. This is found to occur typically in the higher pressure coronal loops. Four long-exposure (30 and 60 s) images were obtained between 17:27:11 UT and 17:30:45 UT. For the present study, we use the same notation to identify the main X-ray structures (B, C, E, W) as Golub et al. did.

2.2. MSDP

On July 11 the Multichannel Subtractive Double Pass (MSDP) spectrograph was operating at the Meudon Solar Tower. Its good spatial resolution ($1''$ – $1.5''$) allows us to see the fine chromospheric structures: fibrils and filaments which will be used for coalignment with the extrapolated magnetic field lines. The MSDP provides nine different wavelength channels of the same two-dimensional area of the Sun (Mein 1977). Some details of the data reduction procedures have been presented in Schmieder, Golub, & Antiochos (1994). The data allow us to reconstruct by interpolation a line profile for each pixel in the field of view. For a given chord ($\Delta\lambda$), the intensity is computed in each pixel, and maps of intensities can be displayed. The standard value for $\Delta\lambda$ is taken equal at 0.6 \AA , which corresponds commonly to the half-width of the H α profile at which the contrast of chromospheric fine structures is generally the best.

2.3. Magnetograph

The magnetograph of the Kitt Peak National Observatory has been described by Livingston et al. (1976). It provides daily full-disk longitudinal magnetic field maps. We use a magnetogram taken on July 11 at 15:55 UT in the 868.8 nm line (Fig. 1b [Pl. 6]). This observation is used for computing the coronal magnetic field lines by extrapolation (see next section). The spatial resolution of the magnetogram is around $1''$. The saturation level of the instrument is about 9000 G; however, because of scattered light, the response of the system inside sunspot umbras was reduced by about a factor of 1.5 (J. Harvey, private communication). Taking this correction into consideration in the spots does not change significantly the extrapolated field lines related to the X-ray-bright loops.

3. ACTIVE REGION 6718

AR 6718 during its disk passage was followed by Debrecen and Potsdam observatories (Aurass et al. 1993). AR 6718 appeared at the east limb as a fairly regular bipolar group, consisting of a round middle-sized spot on the preceding end, together with an elongated (NW-SE) following part with several umbrae in a common penumbra on the other end, and some pores in the middle of the group. The most stable two umbrae are named P0 and F0, as shown in Figure 1a. On July 7, F0 is separated from the rest of the

chain by a light bridge, while the other umbrae of the following part gradually decrease and disperse.

A development of new activity begins from July 8 to 9. In the middle part of the active region, there are new pores forming continually, mostly of positive polarity, which stream forward systematically and eventually coalesce with P0. On July 10, four small umbrae appear and form P1. The counterpart of P1 may be F1 to the south of F0. South of F0, small satellite sunspots of positive polarity emerge, which will correspond to some bright points seen in X-rays during the rocket flight. To the east of F0 we observe a sunspot, P4, which is also associated with X-ray brightenings. At the center of the active region, the small dipole consisting of the pores P2 and F2 is observable only on July 11.

The axis of the new emerging flux regions P1–F1 and P2–F2 has a significant shear compared with the P0–F0 axis (Fig. 2). Their evolution is responsible for the flare occurring on July 10. The greatest evolution is from July 10 to 11 (Aurass et al. 1993). The two ribbons were over P1 and F1, and the flare is likely due to the interaction of P1–F1 with P0–F0. Microwaves at high frequency were recorded. This active region is not very productive of the high level class of flares. Geophysical Data registered the following:

1. July 9, 15:04 M1.2 and some C flares;
2. July 10, 12:26 UT M3.6 and some C flares;
3. July 11, 13:39 and 14:54 UT H α subflares;
4. July 12, some C flares.

During the NIXT flight, no flares occurred in this region, but sheared bright loops were observed over the active

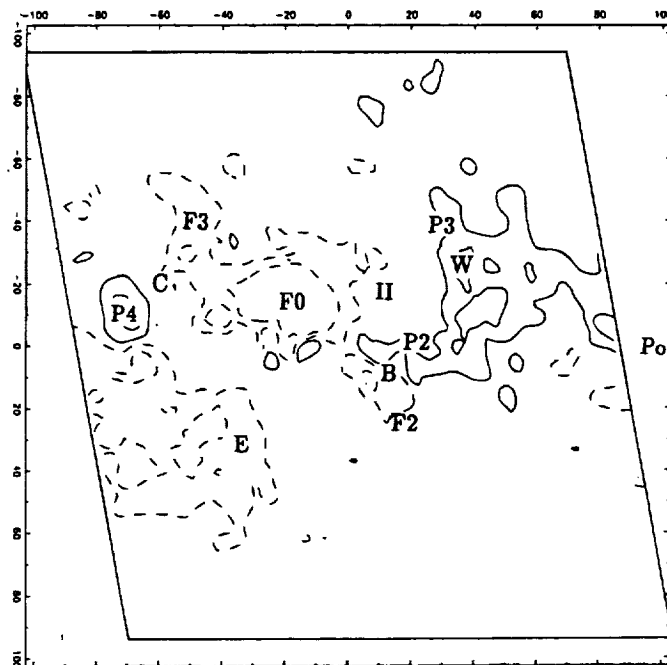


FIG. 2.—Kitt Peak magnetogram of AR 6718 centered on the larger X-ray loops. The labels (P0–P4, F1–F3) designate the sunspots (see Fig. 1) according to their magnetic polarities, “II” locates the H α filament (from Aurass et al. 1993), while B, C, E, W locate the main X-ray structures (from Golub et al. 1994). Continuous and dashed isoncontours represent the longitudinal photospheric field (100 G, 400 G). The scale length unit is in Megameters. North is to the top. The diamond frame delimits the part of the magnetogram shown in the following figures; its borders are parallel to the local parallel and meridian. The extrapolation computation however, is done for a larger region (400 Mm).

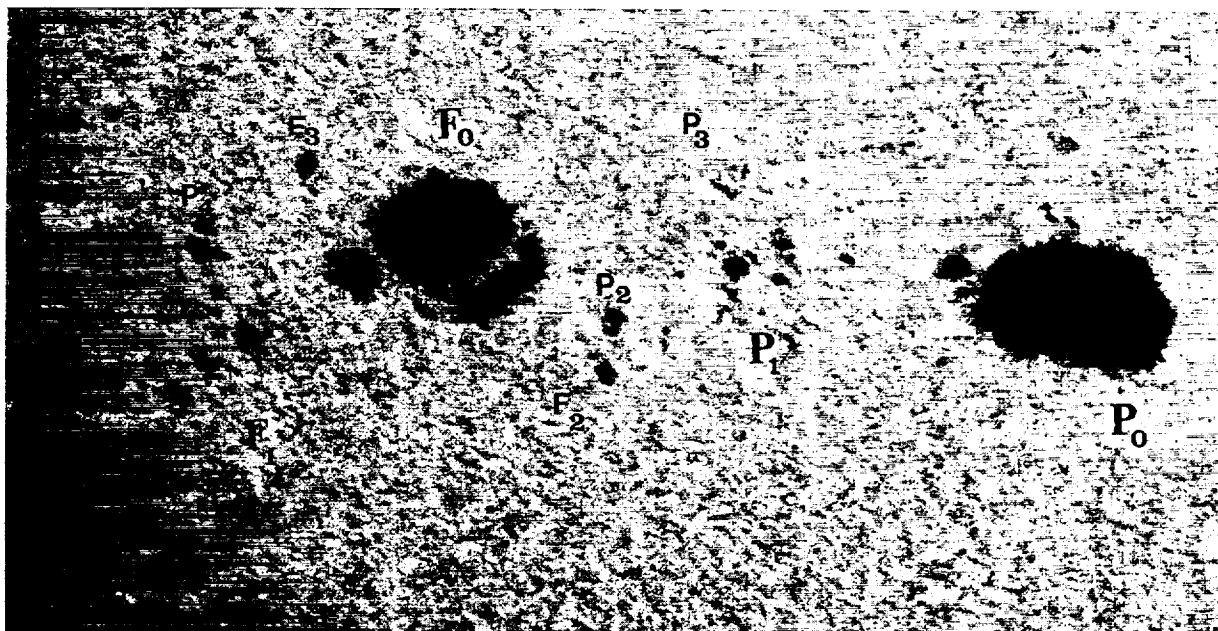


FIG. 1a

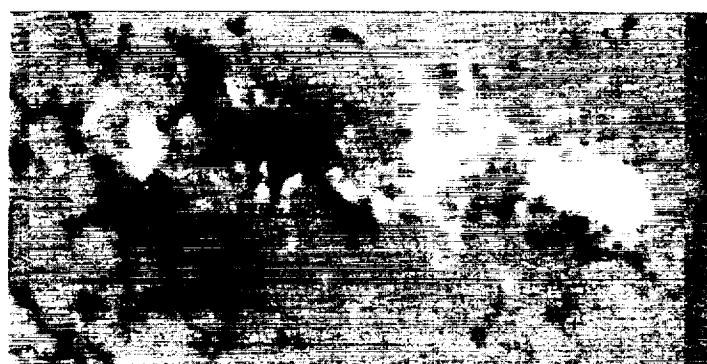


FIG. 1b

FIG. 1.—(a) White-light image of AR 6718 obtained in Debrecen (courtesy of B. Kalman). The letters indicate the sunspots according to their magnetic polarities and relationship. (b) Kitt Peak magnetogram of AR 6718. White/black regions correspond to positive/negative polarities (courtesy of J. Harvey).

SCHMIEDER et al. (see 467, 882)

region. We propose computing the extrapolated magnetic field in the corona from photospheric observations in order to quantify the shear of the coronal loops observed in X-rays.

4. EXTRAPOLATION OF THE MAGNETIC FIELD

The extrapolation code is based on the work of Alissandrakis (1981). The extrapolated fields are calculated under the linear (or constant α) force-free field assumption ($\nabla \times \mathbf{B} = \alpha \mathbf{B}$) using a fast Fourier transform method. (Fig. 3). The required boundary condition is a match to the longitudinal magnetic field values at the photosphere. In order to be able to extrapolate the large-scale structures that are the X-ray-bright loops present in AR 6718, a magnetogram with a large field of view is required. We select a region approximately 400 by 400 Mm in the full-disk Kitt Peak magnetogram. In the figures, we show only a fraction of this field of view, corresponding to the large-scale X-ray loops approximately 100 Mm long, but the magnetic computations are always done using the full selected magnetogram region. This extended region was required to take into account the surrounding field and to decrease the aliasing errors at the borders of the computed region (see Alissandrakis 1981).

The use of magnetograms taken away from the solar disk center requires the elimination of projection effects on the magnetic field and on the spatial coordinates. The full transformation method has been discussed by Gary & Hagyard (1990). On this base, Démoulin et al. (1996) have developed a three-dimensional code for magnetic extrapolation; it has been applied to relate H α flare brightenings to the magnetic topology of the extrapolated field. A more detail discussion of the extrapolation procedure and tests can be found there.

In the present case, the spiral pattern of H α fibrils indicates that the fields at the chromospheric level are not potential (see Aurass et al. 1993 or Fig. 4a [Pl. 7]). The presence of magnetic shear at the coronal level is also evident from the X-ray data (Golub et al. 1994 or Fig. 4c). This contrasts with several previous studies, which concluded that quiet coronal structures are well represented by a potential field extrapolation (Poletto et al. 1975; Sams et al. 1992). Therefore, we have investigated the quality of an extrapolation of the magnetogram with increasing values of the shear (Fig. 3). As is evident, the field lines computed from a potential-field approximation cannot represent both the observed H α and X-ray structures (Figs. 4a and Fig. 4c respectively). As we impose an increasing positive α , the computed field lines become closer to the observed structures. The combination of H α (showing mainly low-lying loops or the feet of loops), X-rays (showing the coronal part of the loops, but with a varying sensitivity along the loop), and extrapolation (giving the entire field line but with uncertainties in the modeling) permit a clarification of the magnetic configuration of AR 6718.

Connections between the strongest polarities (P0–F0) are found in the extrapolation. But while this is the most important magnetic linkage in AR 6718 (both in magnetic flux and intensity), there is no detectable enhanced heating associated with it, either at the chromospheric or coronal level. Small emerging flux regions, like P2–F2 which emerged from July 9 to 11 (see Fig. 2), produce higher levels of X-ray emission (see Fig. 4c), showing that strong magnetic intensity is not a prime requisite for heating. The magnetic loops connecting P2–F2 were found easily in the

extrapolation but not the ones connecting P3 to F3 (suggested by Aurass et al. 1993): field lines starting from P3 always end to the north of F0.

In the east part of the region, both the X-ray (called C in Golub et al. 1994) and H α brightenings located to the southeast of F3 are related to magnetic field lines linking F3 to the southeast negative polarity (called P4 in Fig. 2). It is probably the emergence of this bipole P3–F3, like in the above case P2–F2, that leads to forced reconnection with the overlying magnetic field. Other smaller examples of this phenomenon, at lower spatial scale length, are present to the south of F0 (see the small positive polarities in Fig. 2, which are located in close proximity to the small X-ray brightenings).

AR 6718 is thus formed by a great number of dipoles of different scales which reconnect and brighten when they find their way into the corona. This explanation can hardly be generalized to the spectacular X-ray loops extending from east to west because the polarities look well formed and the X-ray loops seem to fill a large coronal volume. Hereafter we focus on that large feature, keeping in mind that the intense X-ray feature called B (Fig. 2) is linked to the emergence of polarities P2–F2 and only seems to be copatial with the loops extending from west to east because of projection effects.

The hot loops extending from west to east can be found in the field line extrapolation when a positive α is introduced (Fig. 3). However, a unique value of α will not fit all the observed structures. Larger and higher structures are found to be less sheared than the lower ones, and even the very low highly sheared structures seen in H α in the vicinity and in the H α filament (indicated by II in Fig. 2 and visible in Fig. 4a) cannot be reproduced by the extrapolation. Here we see a paradox between the observations and the linear force-free field model. An intrinsic property of the linear force-free field is that large structures are more sheared than smaller ones, implying that long field lines become unrealistically distorted as α is increased (Fig. 3), while short low-lying loops cannot be made as sheared as they are observed to be. The comparison of observations to the extrapolation shows that the coronal magnetic field is not in a state of minimum energy (which is a linear force-free field keeping the total magnetic helicity preserved).

Within the limits of the constant α hypothesis, we can nevertheless reproduce the observed shape of the X-ray loops. The lower loops, corresponding to the dash-dotted curves in Figure 4b, are reproduced in the extrapolation by using $\alpha = 0.019 \text{ Mm}^{-1}$. The larger loops, corresponding to the continuous curves in Figure 4b, are approximately reproduced in the extrapolation with $\alpha = 0.013 \text{ Mm}^{-1}$ ($\approx 30\%$ less than the value requires for the lower X-ray loops). These loops are still highly sheared, and they extend to a large altitude (between 60 and 100 Mm). One can imagine that there are magnetic loops which extend even higher, becoming progressively closer to the potential case, but that such loops are not bright enough to be seen in X-rays. A simplified model of this region is a system of magnetic arcades, highly sheared in the center and becoming progressively less sheared outward (Fig. 5). This is in agreement with the schematic view of the magnetic configuration that Martin (1990) proposed for magnetic configurations supporting filaments.

But why are the loops that extend from west to east bright in X-rays? The brightness of the footpoints both in

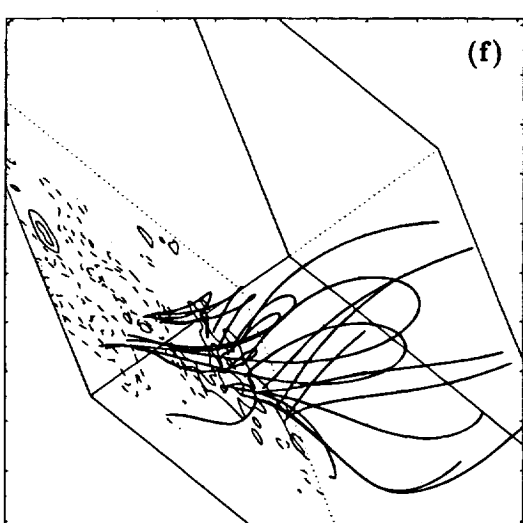
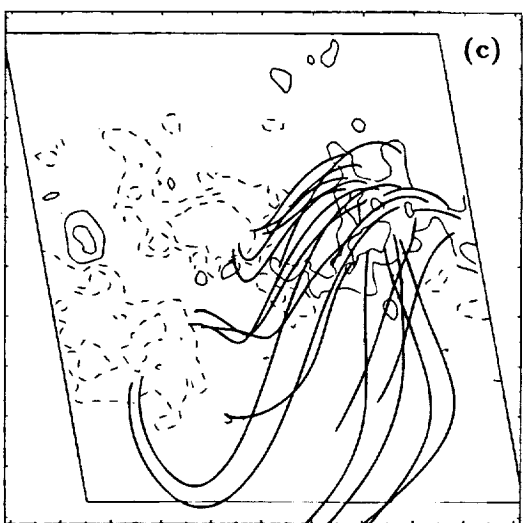
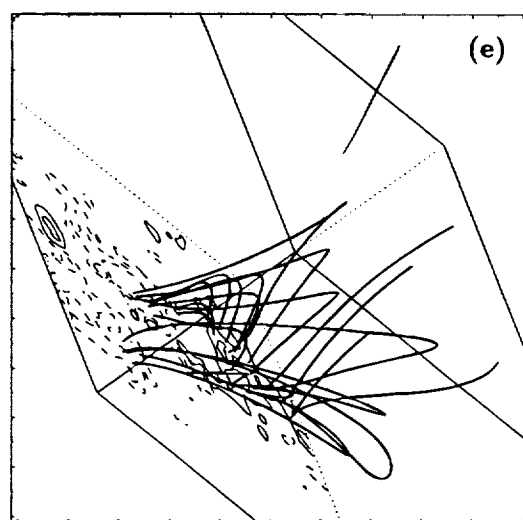
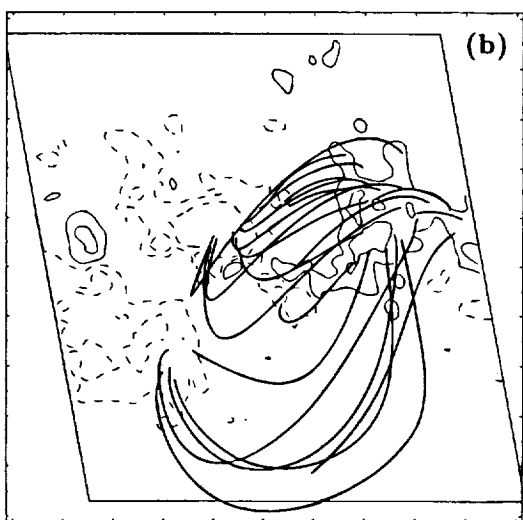
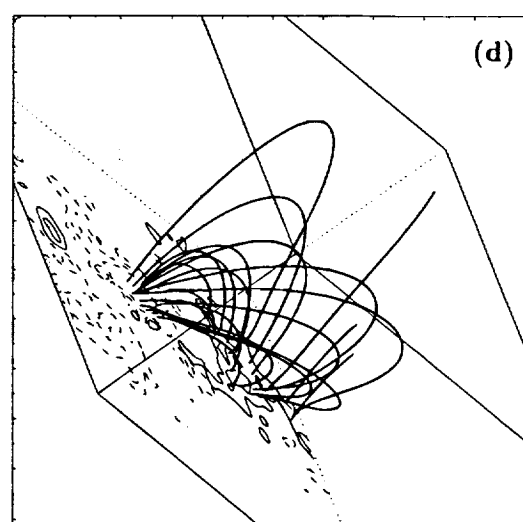
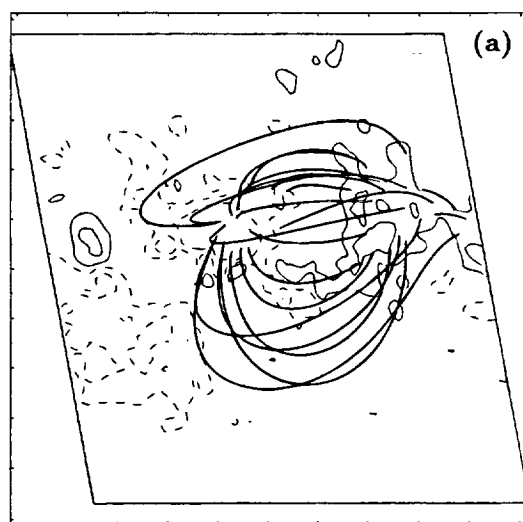


FIG. 3.—Extrapolation of a Kitt Peak magnetogram of the AR 6718 with (a, d) a potential field and a linear force-free field with (b, e) $\alpha = 0.013 \text{ Mm}^{-1}$ and (c, f) $\alpha = 0.019 \text{ Mm}^{-1}$. Field lines have the same starting footpoint in the positive polarity. In (a–c), the point of view of the observer is used (north is to the top), while in (d–f) a side view is shown with the same field lines. The drawing convention for the longitudinal field is the same as in Fig. 2. Only a local view of the region is shown, but the extrapolation is made on a region 4 times larger.

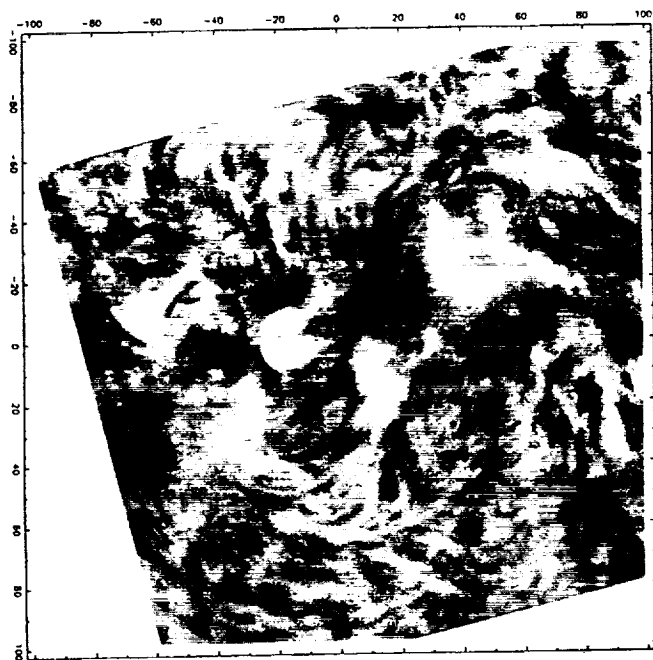


FIG. 4a

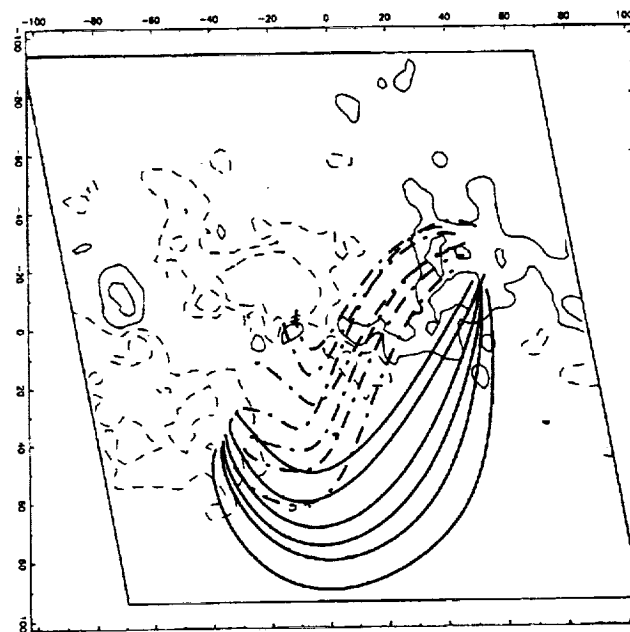


FIG. 4b

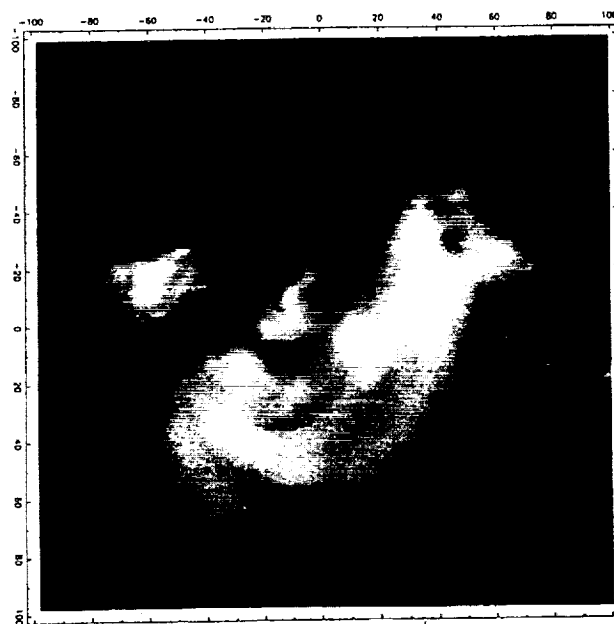


FIG. 4c

FIG. 4.—Comparison of (a) the MDSP and (c) the NIXT observations of AR 6718 to (b) the field line computation. The computed field lines (drawn in continuous style) have a shape compatible with the largest X-ray-bright loops only when a sheared field is used ($\alpha = 0.013 \text{ Mm}^{-1}$). The interpretation of the shape of the lower X-ray loops by field lines (drawn in dash-dotted style) requires a slightly more sheared field ($\alpha = 0.019 \text{ Mm}^{-1}$). The degree of magnetic shear decreases with height from the lower highly sheared H α loops (a) to the higher coronal loops (c).

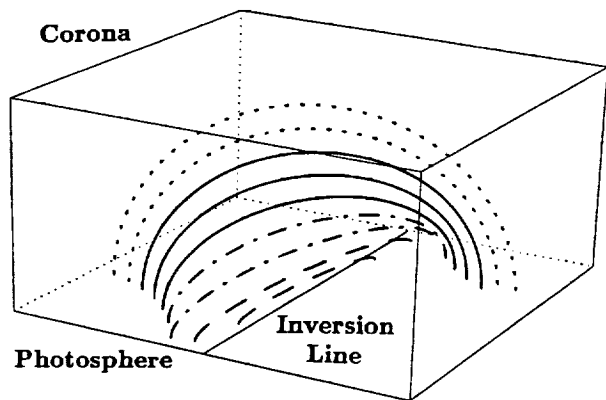


FIG. 5.—Schematic view of the magnetic configuration of AR 6718. The prominence is present in low-lying highly sheared loops (dashed lines), surrounded by arcade loops with magnetic shear decreasing with height (field lines corresponding to the observed X-ray coronal loops are drawn with dash-dotted and continuous lines, while the supposed overlying more potential field lines are drawn with dotted lines).

H α and X-rays delineates approximately the magnetic field map, in particular for the characteristic shape of P3 (Fig. 4). But we have seen above (for loops connecting P0 to F0) that the magnetic field strength is not sufficient to determine the X-ray brightness. The shape of the loop footpoints tells us only that the energy is of magnetic origin and that some other physical parameters should play a key role. It could be the topology of the magnetic field: it is well known that magnetic reconnection occurs on separatrices (see, e.g., Van den Oord 1993; Démoulin 1994). Therefore, we have tried an analysis similar to the one carried out for flares (Démoulin et al. 1996), but without success. This may indicate that the magnetic topology is not well represented by our computation in this highly sheared region (in particular because magnetic shear decreases with height, while the opposite occurs in the linear force-free field extrapolation). But, rather than a localized emission on some loops (or flat volume), the observed X-ray loops on July 11 are seen in a large volume. Another possibility, as suggested in a recent study by Moore et al. (1994), is that X-ray loops are heated at the places at which high shear is present and where underlying flux cancellation occurs. In the present event, flux cancellation may happen in the small bipole (P2–F2) under the large-scale X-ray loops, but it is difficult to believe that such localized and low-lying phenomena can trigger magnetic energy release in the whole large-scale set of X-ray loops.

Rather, we propose that the origin of the observed brightenings of the strongly sheared region are due to the relaxation of the magnetic field as modeled by Heyvaerts & Priest (1984). They described how a magnetic field can lose its excess energy via an MHD turbulent process. In a highly conducting plasma, small-scale processes dissipate magnetic energy much more rapidly than the total magnetic helicity ($H = \int \mathbf{A} \cdot \mathbf{B} dV$ with $\mathbf{B} = \nabla \times \mathbf{A}$; Taylor 1974) or more precisely in the solar context, the total relative helicity (Berger 1985, and references therein). With this constraint, the magnetic field does not relax to a potential state but to a linear force-free state (as was observed in laboratory experiments in spheromacs (Rosenbluth & Bussac 1979). The theoretical final state of the process is a magnetic field with constant α . The gradient of α found in this region (scale

length of 100 Mm) shows that the process of relaxation was not complete at the time of the observations.

5. DISCUSSION AND CONCLUSION

We have used a linear-force-free field extrapolation of the longitudinal field to understand the three-dimensional shape of the observed X-ray and H α structures. The X-ray loops in AR 6718 can be separated in two sets: compact and small loops (with an extension lower than 30 Mm) and large loops (extending to greater than 100 Mm). The emergence of small parasitic polarities and the reconnection of this new magnetic flux with the preexisting coronal magnetic field is the most plausible interpretation for the small-scale X-rays and H α brightenings. The large-scale X-ray loops are anchored in the bipolar field (P1–F1) located in the middle of a stronger bipolar field (P0–F0). Only a set of loops joining P1 to F1 is observed to be bright in X-rays. These loops cannot be related to field lines in the potential approximation, but we show, in a first approximation, that a constant α force-free field extrapolation permits their shape to be recovered, and it shows that the large-scale X-ray loops are highly sheared. However, a second approximation step shows that a different α value is required to fit the field lines both to the lower and upper parts of the X-ray loops. The upper ones are less sheared; they require an α value approximately 30% smaller than for the lower loops. Moreover, an H α filament is present below and the H α fibrils are nearly aligned along the photospheric inversion line, showing that the central part is strongly sheared. Then X-ray and H α observations combined with the magnetic extrapolation show that the central part of AR 6718 is formed by a highly sheared magnetic field, with a magnetic shear decreasing progressively with height (on a scale height of the order of 100 Mm). Therefore, we propose a differential shear configuration for the magnetic field, with a strongly sheared core (Fig. 5), in agreement with the views of Martin (1990) and Antiochos, Dahlburg, & Klimchuk (1994).

The small-scale X-ray loops can find their origin in the reconnection of parasitic flux with the preexisting magnetic flux, while the brightness of the large-scale X-ray loops is puzzling. In the large-scale magnetic configuration, why are only some loops bright? The magnitude of the magnetic field is not the only important parameter of the heating mechanism, since some parts of the corona have much higher fields while they do not emit in X-rays, and the X-ray-bright loops do not have footpoints in the main sunspots (see also Sams et al. 1992). However, we can surmise that the mechanism is of magnetic origin, since the brighter loops are associated with the photospheric magnetic polarities. Are the observed loops bright due to reconnection between the main bipoles (P0–F0) and (P1–F1)? Within the limits of the magnetogram calibration and the linear force-free field assumption, the topological computations have failed to explain the position of the large X-ray loops. Moreover, the observed spatial extension of the bright loops rules out a mechanism localized on a very flat volume, like reconnection on two intersecting separatrices. The mechanism for heating these quiet X-ray loops seems to be different from that found for flares (Démoulin et al. 1996).

We find that the brightest soft X-ray emission corresponds to a nonpotential state of the magnetic field, in which the strongest X-ray emission is associated with the largest shear (this, however, does not hold for the highly

sheared field lines containing the filament). This agrees with Moore et al. (1994), who report that the coronal heating is enhanced at the sites of strong shear. This argument receives additional indirect support from the measurement of the cross-sectional variation of the loops observed by NIXT (Golub 1991) and by the *Yohkoh* SXT: the thickness variation along the loop was found to be only 10%–20% at most. McClymont & Mikic (1994) demonstrate that this observation is consistent with the characteristics of current carrying field lines in a highly sheared active region (using an MHD code for the extrapolation). The relationship between electric currents and X-ray brightness (and therefore heating) is, however, still debatable. Metcalf et al. (1994) find no correlation between the locations of bright X-ray structures and the sites of sustained strong photospheric currents; the field lines connecting the upward/downward current densities are found to be unassociated with the brightest SXR emission over a 7 day period of observation. For AR 6718, present vector magnetographs like the one in Potsdam are not sensitive enough in the linear polarization to derive electric currents at the feet of the large X-ray loops at which the strength of longitudinal magnetic field is low (≤ 400 G at the magnetograph resolution).

The central part of AR 6718 is formed by a highly sheared magnetic field, with a magnetic shear decreasing progressively with height. This differential shear may be at the origin of the observed loop brightening, triggering a relaxation process as proposed by Heyvaerts & Priest (1984).

With the high magnetic Reynolds number of the solar corona, the total magnetic helicity of the magnetic field is preserved. With this constraint, a stressed magnetic field relaxes, via MHD turbulence, to the linear force-free field compatible with the boundary conditions (mainly the photospheric vertical flux distribution). Following Moore et al. (1994), the magnetic shear could be a necessary condition, but not a sufficient one for heating. A differential magnetic shear is likely to be another condition. Finally, a multitude of reconnecting current sheets, the dissipation of a large number of small-scale currents, or a wave heating mechanism are possible alternatives, but the present data cannot permit a definitive selection of all the possible candidates for coronal heating mechanisms.

The authors wish to thank A. Hofmann and H. Aurass for fruitful discussions, B. Kalman for providing the white-light pictures from Debrecen Observatory, J. Harvey for providing the magnetogram from Kitt Peak (the NSO/Kitt Peak data used here are produced cooperatively by NSF/NAO, NASA/GSFC, and NOAA/SEL), and R. Hellier and C. Coutard for the MSDP observations at the Meudon Solar tower. The MSDP observations have been digitalized at the microdensitometer MAMA of the Observatoire de Paris. B. S. thanks the Smithsonian Institute for supporting her stay in Cambridge (US). L. G. was supported in part by NASA grant NAGW-4081 to the Smithsonian Institution.

REFERENCES

- Alissandrakis, C. E. 1981, *A&A*, 100, 197
 Antiochos, S. K., Dahlburg, R. B., & Klimchuk, J. A. 1994, *ApJ*, 420, L41
 Aurass, H., Hofmann, A., Magun, A., Soru-Escut, I., & Zlobec, P. 1993, *Sol. Phys.*, 145, 151
 Berger, M. A. 1985, *ApJS*, 59, 433
 Démoulin, P. 1994, in *Advances in Solar Physics*, ed. G. Belvedere, M. Rodono, & G. M. Simnett (Berlin: Springer), 121
 Démoulin, P., Bagalá, L. G., Mandrini, C. H., Hénoux, J. C., & Rovira, M. G. 1996, *A&A*, submitted
 Gary, G. A., & Hagyard, M. J. 1990, *Sol. Phys.*, 126, 21
 Gary, G. A., Moore, R. L., Hagyard, M. J., & Haisch, B. M. 1987, *ApJ*, 314, 782
 Golub, L. 1991, in *Mechanisms of Chromospheric and Coronal Heating*, ed. P. Ulmschneider, E. R. Priest, & R. Rosner (Berlin: Springer), 115
 Golub, L., Zirin, H., & Wang, H. 1994, *Sol. Phys.*, 153, 179
 Hannakam, L., Gary, G. A., & Teuber, D. L. 1984, *Sol. Phys.*, 94, 219
 Heyvaerts, J., & Priest, E. R. 1984, *A&A*, 137, 63
 Livingston, W. C., Harvey, J., Slaughter, C., & Trumbo, D. 1976, *Appl. Opt.*, 15, 40
 Martin, S. 1990, in *IAU Colloq. 117, Dynamics of Quiescent Prominences*, ed. V. Ruzdjak & E. Tandberg-Hanssen (Lecture Notes in Physics, Vol. 363), 1
 McClymont, A. N., & Mikic, Z. 1994, *ApJ*, 422, 899
 Mein, P. 1977, *Sol. Phys.*, 54, 44
 Metcalf, T. R., Canfield, R. C., Hudson, H. S., Mickey, D. L., Wülser, J. P., Martens, P. C. H., & Tsuneta, S. 1994, *ApJ*, 428, 860
 Metcalf, T. R., Jiao, L., McClymont, A. N., Canfield, R. C., & Uitenbroek, H. 1995, *ApJ*, 439, 474
 Moore, R. T., Porter, J., Roumeliotis, G., Tsuneta, S., Shimizu, T., Sturrock, P. A., & Acton, L. W. 1994, *Proc. Kofu Meeting (NRO Rep. No. 360)*, 89
 Peres, G., Reale, F., & Golub, L. 1994, *ApJ*, 422, 412
 Poletto, G., Vaiana, G. S., Zombeck, M. V., Krieger, A. S., & Timothy, A. F. 1975, *Sol. Phys.*, 44, 83
 Rosenbluth, M. N., & Bussac, M. N. 1979, *Nucl. Fusion*, 19(4), 489
 Sakurai, T. 1982, *Sol. Phys.*, 76, 301
 Sakurai, T., & Uchida, Y. 1977, *Sol. Phys.*, 52, 397
 Sams, B. J. III, Golub, L., & Weiss, N. O. 1992, *ApJ*, 399, 313
 Schmieder, B., Dere, K. P., Raadu, M. A., Démoulin, P., & Alissandrakis, C. E. 1990, *Adv. Space Res.*, 10(9), 195
 Schmieder, B., Golub, L., & Antiochos, S. K. 1994, *ApJ*, 425, 326
 Spiller, E., McCorkle, R. A., Wilczynski, J. S., Golub, L., Nystrom, G., Takacs, P. Z., & Welch, C. 1991, *Opt. Eng.*, 30, 1109
 Taylor, J. B. 1974, *Phys. Rev. Lett.*, 33, 1139
 Van den Oord, G. H. J. 1993, *Adv. Space Res.*, 13(9), 143

DIFFICULTIES IN OBSERVING CORONAL STRUCTURE

L. GOLUB

Smithsonian Astrophysical Observatory, Cambridge, MA 02128, U.S.A.

(Received 3 July 1966; accepted 29 October 1996)

Abstract. There has developed in recent years a substantial body of evidence to indicate that the temperature and density structure of the corona are far more complicated than had previously been thought. We review some of the evidence and discuss some specific examples: observations of a limb flare, showing that the cool $H\alpha$ material is *cospatial* with the hot X-ray emitting material; simultaneous NIXT and *Yohkoh* SXT observations of an active region, showing that loops seen in one instrument are not seen in the other, and that the effect works in *both* directions; comparisons of extrapolated magnetic field measurements to the observed coronal structure, indicating that neither potential nor constant- α force-free fits are adequate. We conclude with a description of two new instruments, the TRACE and the TXI, which will help to resolve some of these difficulties.

1. Overview

The importance of magnetic fields in determining the structure of the solar outer atmosphere has long been recognized. Billings (1966) notes that magnetic fields 'are employed, as a matter of fact, to explain all departures from a nonspherical [sic] distribution of matter in the corona, including the loop structure of the corona over active regions...' Observations from sounding rockets in the late 1960s and early 1970s provided convincing evidence that loops structures, apparently outlining the magnetic field direction, are fundamental (Vaiana, Krieger, and Timothy, 1973) and the *Skylab* observations in 1973-1974 provided the impetus for constructing atmosphere models in which loop 'mini-atmospheres' are the fundamental constituent of the inner corona (Rosner, Tucker, and Vaiana, 1978; Craig, McClymont, and Underwood, 1978).

This atmosphere is dynamic and constantly varying. Low (1990) notes that the solar atmosphere is never truly quiescent or static, but adds that for the purpose of building models idealized static states may be used as an approximation to the physics underlying the apparent stability of long-lived structures. The extremely dynamic nature of the corona has been shown most effectively by the Soft X-ray Telescope (SXT) aboard the *Yohkoh* satellite: repeated transient loop brightenings in active regions (Shimizu *et al.* 1992), continual rapid expansion outward of structures at the tops of active regions (Uchida *et al.*, 1992), jets of X-ray emission, apparently associated with reconnection events (Shibata *et al.*, 1992), among others.

Thus, it is already clear that the simplest models of the corona – spherical or plane-parallel – are of limited applicability for interpreting the actual observations, and that the simplest loop atmosphere models – static loops – are also of limited usefulness. To these complications, we will add an additional set of worries, by

Table I
Observational questions about the solar corona

Q1.	Is the corona hot or cold at a given point in space?	A1.	Depends on the viewing method.
Q2.	Where is the 'base' of the corona?	A2.	Meaningful only for individual loops and probably unanswerable.
Q3.	What is the transverse scale size of coronal structures?	A3.	Our knowledge is limited by present instrumental resolutions.
Q4.	What is the relation between the coronal B and X-ray emission?	A4.	Data do not provide sufficient constraints.
Q5.	What does the hot corona look like?	A5.	Depends on the viewing method.

showing that it is not at all clear that we are even now in a position to say that we know what coronal loops look like, or to know how the real corona is constructed of such loops.

2. Case Studies

In order to illustrate the difficulties alluded to in the Overview, we will examine five specific 'case studies,' each involving a seemingly reasonable question about the corona. The questions addressed by these studies are listed in Table I, along with the answer to each question. The latter will be explained in the course of discussing each case. These examples are all taken from work related to flights of the Normal Incidence X-ray Telescope (NIXT) sounding rocket payload (Golub *et al.*, 1990) during the years 1989–1993.

2.1. A LIMB FLARE

On 11 Sept. 1989, the NIXT rocket was launched at the start of a small flare (GOES classification C5). However, during the five-minute flight, a second flare began in an active region at the limb (Herant *et al.*, 1991). Examination of the GOES X-ray light curves (Figure 1) indicates that the limb flare began at about 16:36 UT during the decay phase of the larger on-disk flare. The NIXT observations also began at 16:36 UT, with the last image taken at 16:41:35 UT; the peak of the limb flare in X-rays is at $\sim 16:42$ UT. Thus, the NIXT coverage could not have been better-timed.

Figure 2 shows simultaneous $H\alpha$ and X-ray images of the flare at the time of the peak. The most striking aspect of this event seems to be the nearly identical size, shape and location of the flare in the two wavelength regimes. This similarity is confirmed by a cross-correlation between the two datasets, shown in Figure 3. The contour lines show the X-ray brightness and the shaded region shows the H brightness: the two overlap to within the accuracy of alignment. Thus it would

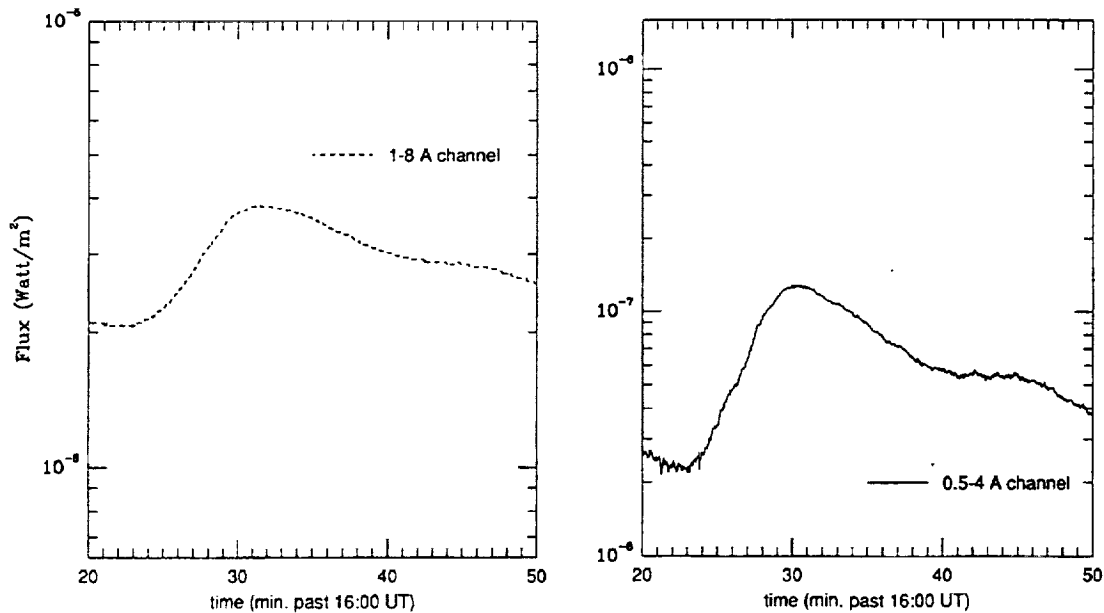


Figure 1. GOES 1-8 Å and 0.5-4 Å X-ray plots for 9 November, 1989.

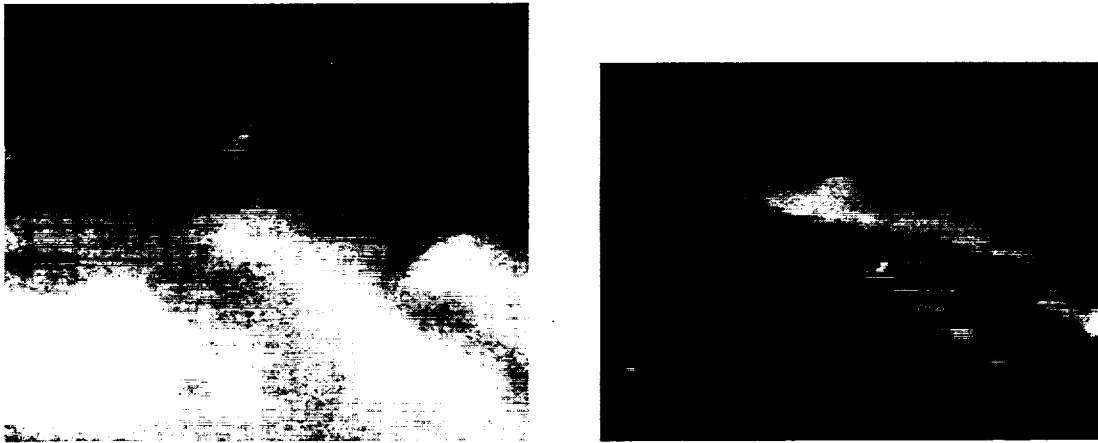


Figure 2. Simultaneous H α and NIXT X-ray images of a limb flare.

appear that the corona is both hot (X-ray) and cool (H α) at the same place at the same time.

Possible explanations exist, of course, for this apparent contradiction. It is possible that the X-ray emission originates from a thin shell ahead of the advancing H α region. Alternatively, hot and cool material may be intermingled on small spatial scales within the observed regions. The problem is not to come up with an answer, it is to come up with a correct answer.

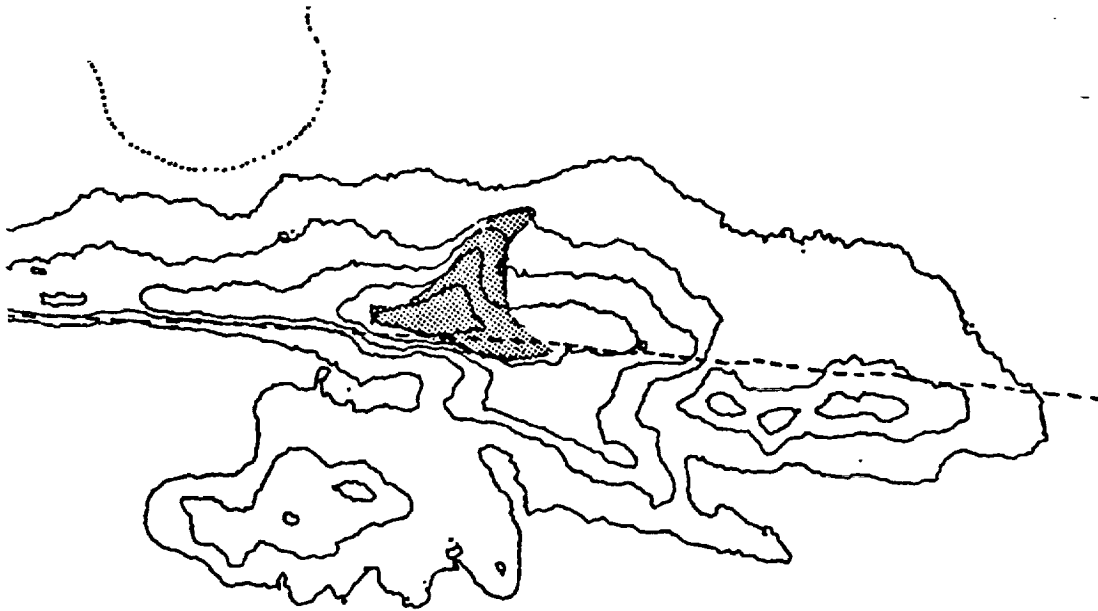


Figure 3. Relative positions of X-ray event and H α material.

2.2. SIMULTANEOUS WHITE-LIGHT AND X-RAY IMAGING

Plane-parallel, or spherically symmetric models of the outer solar atmosphere treat the relation between temperature and height as one-dimensional, although not monotonic since the temperature at first increases with height but then decreases again. With the advent of loop model atmospheres, as described above, this fundamental view did not change in essence, but the temperature vs height relation is transplanted into each loop instead of into the atmosphere as a whole. However, a flight of the NIXT payload on 22 February 1991 provided a unique dataset which shows that a more complicated geometry is required in order to explain the observations.

The multilayer mirrors used in the NIXT to provide X-ray imaging also reflect visible light with $\approx 50\%$ reflectivity. In order to record only the (much fainter) X-ray image, two stages of visible-light rejection are employed: an entrance aperture filter, which cuts the visible to $\approx 1\%$ and a focal plane filter, which provides 10^9 reduction in the visible. During the launch phase of the February 1991 flight, a portion of the entrance aperture filter broke. The instrument, however, was designed so that the focal plane filter acts as back-up in the event of just such a failure. Thus, because the X-rays and the visible are reflected in the same way from the same mirror at the same time, we obtained simultaneous images of the visible disk and the corona. These are automatically coaligned and have the same plate scale, so that high precision (<1 arc sec) comparison between the two can be made.

Figure 4 shows a portion of the east limb from one of the exposures obtained on that flight. Note that there is a dark band at the limb, between the white-light solar limb and the bright coronal X-ray emission. We note several features of this

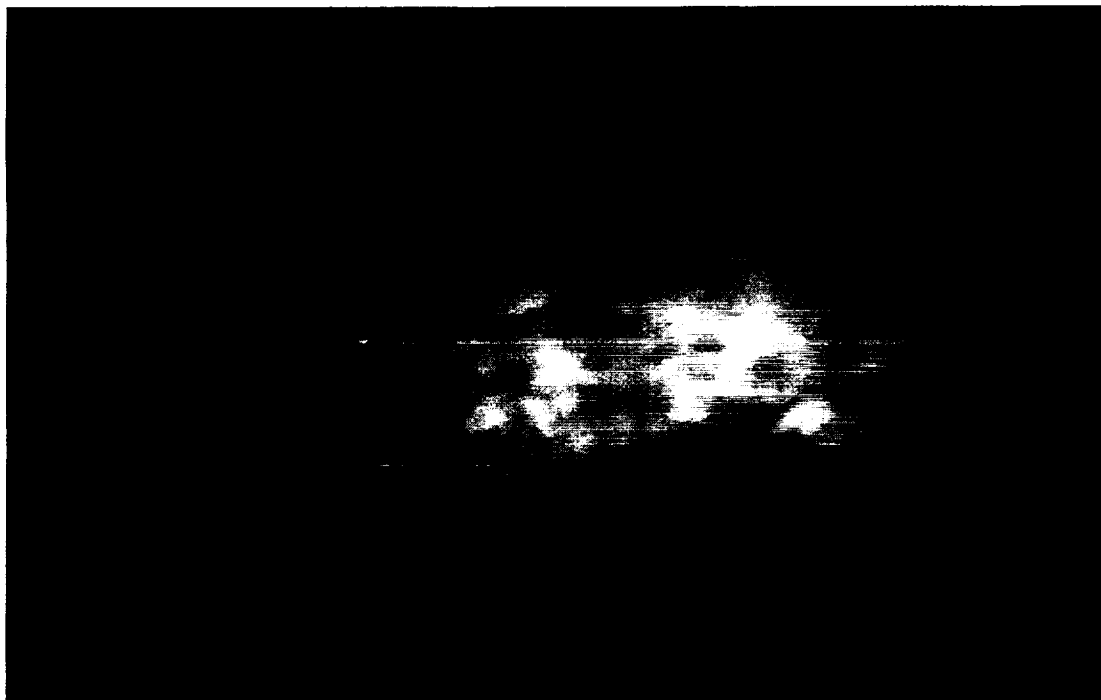


Figure 4. Portion of a combined NIXT/white-light image, showing a gap between the visible limb and the 'base' of the corona, 22 February, 1991.

gap: (1) it is most clearly evident when there is an X-ray emitting region behind the limb and no emitting region in front of the limb; (2) the thickness of the gap varies between equator and poles, or between active regions and large scale 'quiet' regions; (3) at both the inner (white light) and outer (X-ray) heights, the gap is quite sharp. The question we will address is, how is this gap to be interpreted?

The data from this flight have been analyzed by Daw, DeLuca, and Golub (1995), who find that a model in which the corona is viewed as consisting of a homogeneous set of loops, with temperature varying as a function of height in a uniform manner (Figure 5(a)) is not consistent with the data. In order to explain what is seen, it is necessary to use a model in which hot loops penetrate downward into an atmosphere having cool spicular material penetrating upward (Figure 5(b)). The two types of loops do not connect physically, but are interspersed along the line of sight. Thus, the gap is interpreted as the upward extent of spicular material, viewed along the line of sight at the limb and absorbing the X-rays emanating from loops behind the spicules.

We note that the soft X-rays in the NIXT data are strongly absorbed in spicular material, with about 10 arc sec path length required for e^{-1} absorption. The variation in thickness of the band indicates that spicules may extend farther in open field (e.g., coronal hole) regions than in higher temperature closed-loop regions, as reported by Huber *et al.* (1974). This interpretation of the NIXT data suggests that the footpoints of coronal loops cannot, in principle, be seen. When viewed at the limb,

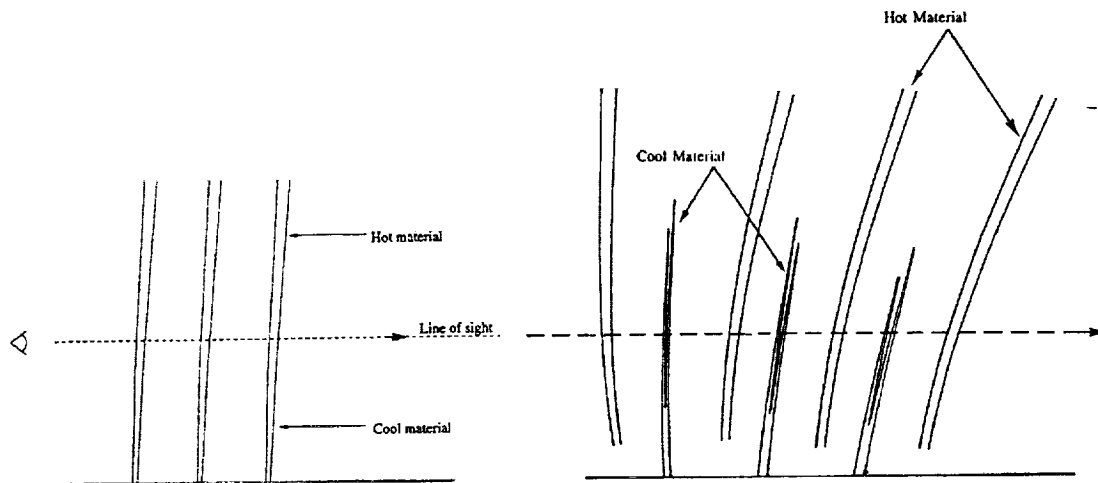


Figure 5. Two loop model atmospheres offering alternative explanations of the gap seen in Figure 4. Modified plane-parallel model on left does not fit the data.

they are obscured by the intervening spicule material; when viewed from above, the projection angle is such that the height of the coronal 'base' is very poorly determined. Depending upon the relative spatial density of hot vs cool structures, there may be a small range of locations near the center of the disk which allow for both viewing the loops at an angle and for viewing them unobstructed. However, this is not yet known.

2.3. ACTIVE REGION FINE STRUCTURE

The progress in X-ray optics, when applied to solar coronal imaging, has consistently revealed coronal fine structure down to the resolution limit of the observing instruments (see, e.g., articles by Giacconi, Golub, and Walker *et al.* in Linsky and Serio, 1993). An example is shown in Figure 6, a coronal X-ray image from the NIXT instrument, obtained on 11 July, 1991. There is clearly fine structure prevalent everywhere in the image and photographic analysis indicates that it reaches the combined limit set by the film and by the pointing stability of the rocket.

A quantitative analysis of the fine structure of several active regions observed by the NIXT was carried out by Gómez, Martens, and Golub (1993). By Fourier analyzing the images, they find a broad, isotropic power-law spectrum for the spatial distribution of soft X-ray intensities. The spectrum has a slope of $\alpha \approx -3$, which extends down to the resolution limit of the instrument at ≈ 0.75 arc sec.

A similar result has been obtained by Martens and Gómez (1992) from analysis of *Yohkoh* SXT data: the Fourier transform distribution is a power law (with somewhat smaller slope of ≈ -2.4) which extends down to the Nyquist frequency. Thus, for both cases in which the procedure has been carried out, the spatial structuring of the corona is seen to be limited by the resolution of the imaging instrument. The implication, since the Sun does not know what instrument we are

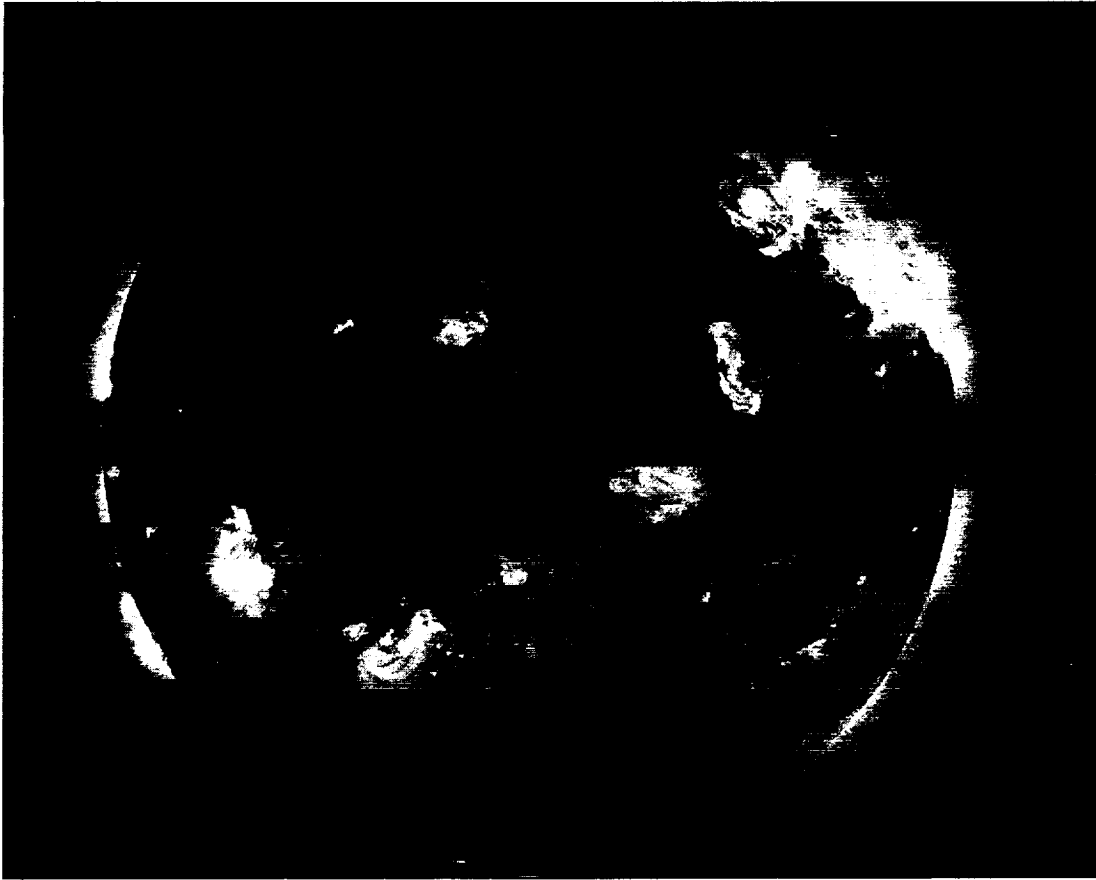


Figure 6. 11 July, 1991 NIXT image.

using to observe it, is that we have not yet fully resolved the coronal fine structure. Thus, the answer to Question 3, 'What is the transverse scale size of coronal structures?', is that we do not yet know.

2.4. MAGNETIC FIELD EXTRAPOLATION VS OBSERVED STRUCTURE

There have been only a limited number of attempts in recent years to carry out direct comparisons between high resolution coronal observations and magnetic field extrapolations, if we exclude attempts to explain the onset of flares by testing the non-potentiality of fields. For non-flaring regions, i.e., normal coronal structure, Poletto *et al.* (1975) and Sakurai and Uchida (1977) had reasonable success at the level of late 1960s and early 1970s resolution. More recently Sams, Golub, and Weiss (1993) found a general agreement between extrapolations and the structures seen in the NIXT, although close examination shows that the agreement is quite poor in detail. Metcalf *et al.* (1994) conclude, from comparison of vector magnetograph data (giving the locations of vertical currents) with *Yohkoh* SXT coronal data, that there is a very poor spatial and temporal correlation between the locations of the currents and the locations of bright coronal structures.

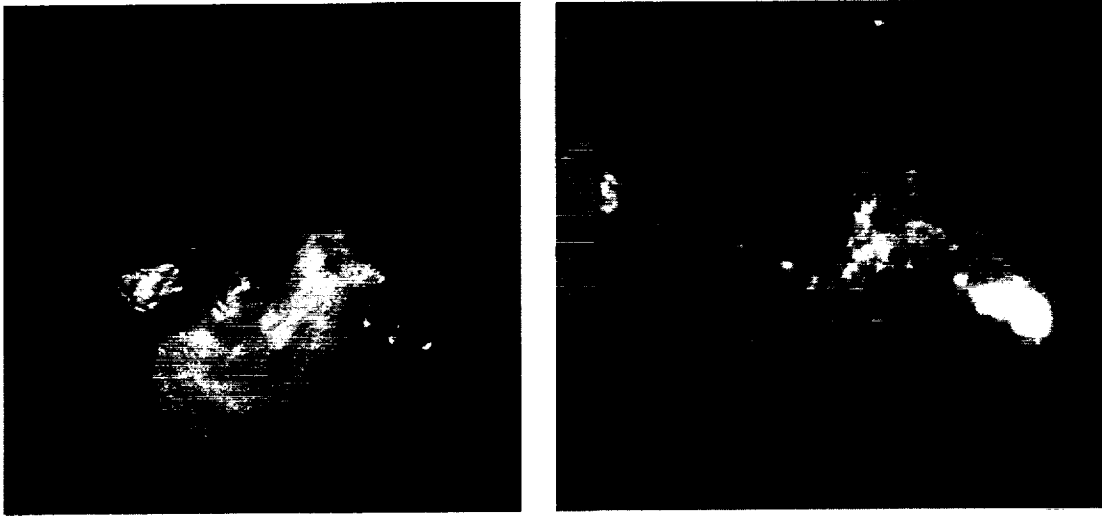


Figure 7. NIXT X-ray image of AR 6718 and KPNO magnetogram of the region.

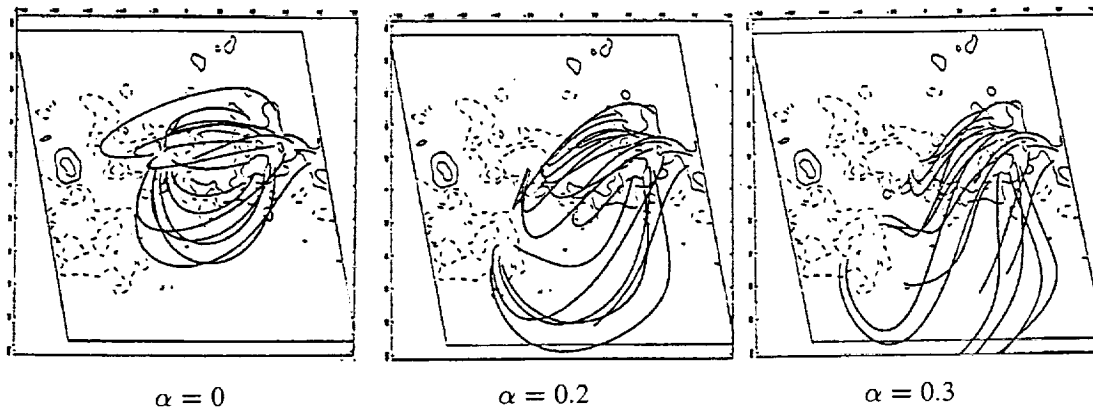


Figure 8. Magnetic field extrapolations of AR 6718, with three values of α .

In a recent study, Schmieder *et al.* (1996) have used high resolution NIXT data combined with Kitt Peak magnetogram and Multi-channel Double Pass (MSDP) spectrograph data, to study in more detail the relationship between the observed structure and the type of magnetic field extrapolation employed. The extrapolation code is based on the work of Alissandrakis (1981) as modified by Démoulin *et al.* (1996). A single active region, AR 6718 on 11 July, 1991, was chosen for study; an X-ray image of the region and the corresponding portion of the magnetogram are shown in Figure 7.

The first result is that a potential-field extrapolation does not represent the observed coronal structure at all, and that even a constant- α force-free field extrapolation is not adequate. Figure 8 shows extrapolations using three values of α . The left-most panel shows $\alpha = 0$, i.e., a potential field. Note that the connectivity of the field lines is entirely different from that of the observed structures. The two force-free fits in the middle and right-hand panels match portions of the region,



Figure 9. Comparison between *Yohkoh* (top) and NIXT (bottom) observations of an active region; arrows indicate structures seen in one of the instruments but *not* seen in the other.

but neither one in itself is a good fit. What we find is that the inner portion of the active region is well matched by the larger value of α while the outer portion of the region is matched by a lower α .

A possible interpretation of this result is that there is, with time, a relaxation of the magnetic field, as proposed by Heyvaerts and Priest (1984). In a highly-conducting plasma, small-scale processes dissipate magnetic energy much more rapidly than helicity $H \equiv \int \mathbf{A} \cdot \mathbf{B} \, dV$ (Taylor, 1974; Berger, 1985). With this constraint the magnetic field does not relax to a potential state, but to a linear force-free state. The gradient of α found in this region may be indicative of this ongoing relaxation process.

2.5. *Yohkoh* SXT vs NIXT COMPARISON

In April 1993 the *Yohkoh* SXT carried out a special observing sequence simultaneous with a flight of the NIXT rocket. An initial comparison of the two datasets was carried out by Yoshida *et al.* (1995) for a quiet corona region. Because the SXT temperature response is somewhat harder than that of the NIXT (>2.5 MK for SXT vs $1-3$ MK for NIXT) it was expected that the SXT would see the hotter top portions of coronal loops while the NIXT would see the lower portions or the footpoints. This was indeed generally seen to be the case in that study.

However, subsequent evaluation of the one active region on the disk on that day is showing a completely different and unexpected result. One expects that 'all X-ray images are alike,' so that the two should show roughly similar structures. Viewed from a distance, the two observations seem to be showing the same coronal features. However, detailed examination shows some remarkable discrepancies between the two.

Figure 9 shows the comparison of NIXT and *Yohkoh* SXT observations, with arrows pointing to three locations in the region. These are places where a structure or set of structures is visible in one of the images and *entirely invisible* in the other; the effect works both ways. Thus, if only one of these images were available, we would draw erroneous conclusions about the coronal structure, since there would be no indication at all that some structures are present.

The seriousness of this problem is obvious: if we intend to study the formation, stability and dynamics of coronal structures, one must first be able to see them. A partial solution to this problem is described in the next section.

3. Some Partial Solutions

The above discussion provides only a partial listing of some of the problems we are encountering in attempting to study the formation, heating, structuring and dynamics of the solar corona. In this section we describe two new instruments which will help to solve, or at least advance, some of these problem areas. The

TRACE instrument will have the highest spatial resolution ever used to observe the corona, as well as the ability to discriminate multiple temperature regimes and to view the atmosphere from the upper chromosphere up into the active region corona. The TXI is a rocket-borne payload which will have the capability of observing the entire sequence of successive ionization stages of a single element from $<10^6$ K to $>3 \times 10^6$ K, and will also determine flow velocities at these temperatures.

3.1. TRACE

The Transition Region And Coronal Explorer (TRACE) is designed to explore quantitatively the connections between fine-scale magnetic fields at the solar surface and the associated plasma structures in the solar outer atmosphere. The TRACE instrument uses multiple UV and normal-incidence XUV channels to collect images of atmospheric plasma from 10^4 K to 10^7 K. Many of the physical problems that arise in this portion of the atmosphere – plasma confinement, reconnection, wave propagation, plasma heating – arise throughout space physics and much of astrophysics as well. Although recent progress in, e.g., numerical MHD simulations has been substantial (viz., Low, 1990), use of these models requires close guidance by the observations, because the enormous range in parameter scale sizes cannot be realized in the computations.

The telescope provides true 1 arc sec resolution (1 pixel is 0.5 arc sec) and temporal resolution as short as a fraction of a second for bright sources. Table II lists the operating spectral bands, the associated temperatures and the portions of the atmosphere covered. The instrument uses four normal incidence coatings, one for broadband UV and three for narrow band XUV operation. The UV channel includes a set of narrow-band filters at the focal plane, thereby allowing sub-channels which detect portions of the atmosphere from the photosphere to the transition region. Selection of the XUV channels is based on a thorough analysis carried out by Golub, Hartquist, and Quillen (1989), who analyzed the spectral region accessible to normal incidence techniques and determined the best lines to use for particular atmospheric features of interest.

TRACE is launched on a Pegasus-XL into a polar, Sun-synchronous orbit, thereby providing continuous observation of the Sun. Continuous observing for about 8 months is planned over a 1-year baseline mission. TRACE produces data complementary with SOHO, and planning of the TRACE daily observations is being coordinated with those of SOHO.

The main components of the TRACE instrument are shown in Figure 10. The TRACE instrument consists of a 30-cm diameter Cassegrain telescope and a filter system feeding a CCD detector. Each quadrant of the telescope is coated for sensitivity to a different wavelength range. Light entering the instrument passes first through an entrance filter assembly which transmits only UV and soft X-ray radiation, thus blocking the solar heat from reaching the mirrors. A large rotating

Table II
TRACE spectral regions and observing parameters

Central wavelength (Å)	Width (Å)	Ion	Location
2500	Broad	Continuum	Photosphere
1700	Broad	$T_{\min}/\text{Chrom.}$	
1570	30	C I, Fe II, Cont.	Photosphere
1550	30	C IV	Transition region
1216	84	H $L\alpha$	Chromosphere
284	14	Fe XV	Corona
195	10	Fe XII	Corona
		(+Fe XXIV)	Flares
171	9	Fe IX	Corona

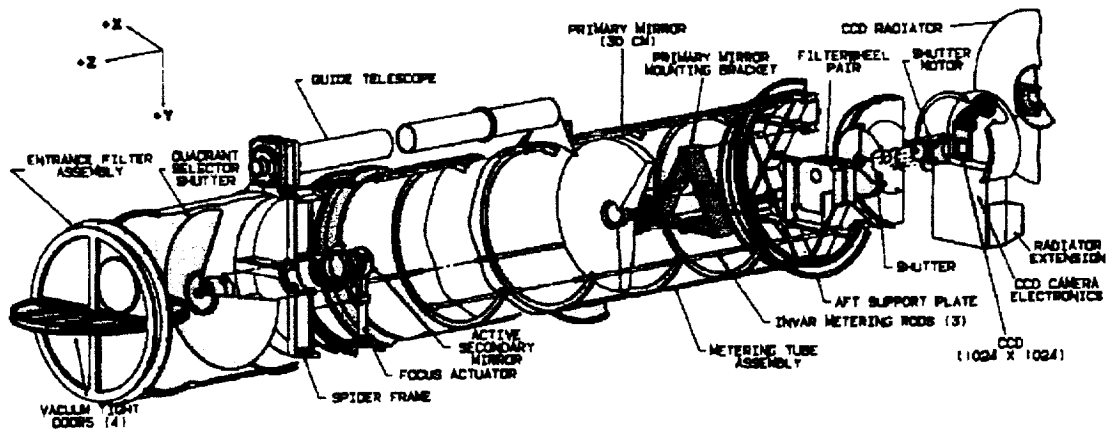


Figure 10. Major system components of the TRACE instrument.

quadrant shutter selects one quadrant at a time for viewing. The secondary mirror of the telescope is active, to correct for pointing jitter to better than 0.1 arc sec.

The converging beam from the secondary mirror passes through the central hole in the primary, where it encounters two filter wheels in series, each having three filters and one open position. These wheels contain both the XUV light-blocking and the UV passband filters. Finally, there is a focal plane shutter and a 1024×1024 CCD, for a field of view of 8.5×8.5 arc min. Mosaic observations are planned, for larger field and daily full disk data-taking. The TRACE launch is late in 1997, and mission lifetime is at least 8 months. Thus it will be observing during the rise phase of the new solar cycle.

Some of the scientific objectives of the mission are:

- Magnetic field structure and evolution.
- Coronal heating and magnetic fields.
- Onset of coronal mass ejections.
- Variability of X-ray bright points.

The mission and its objectives are described in more detail in Tarbell *et al.* (1994).

3.2. TXI

The Tuneable X-ray Imager (TXI) is a high-resolution coronal imaging instrument which has the ability to produce near-monochromatic images tuneable over a range of XUV wavelengths. The present design covers the wavelength range 170–220 Å, which includes the strong series of iron lines from Fe IX through Fe XIV, inclusive. Thus, the problem of ‘missing’ structures is solved, for the temperature range $\log T = 5.8\text{--}6.4$, because all of the successive ionization stages are isolated and recorded.

Figure 11 shows a schematic layout of the instrument. Spectral isolation is achieved by using a double-crystal monochromator, which feeds a broadband telescope, coated with an XUV multilayer having $\Delta\lambda \sim 30\text{ Å}$ (FWHM). The monochromator is made as narrow-band as possible, which in this instance is $\approx 4\text{ Å}$, and it is tuned by rotating the two plane mirrors in parallel. A Cowan–Golovchenko arrangement is used (Cowan, 1983), which has the highly desirable property that the entrance and exits beams stay fixed during tuning. Thus, there is no image motion in the focal plane as the wavelength is changed.

Table III shows the strongest lines in the TXI passband. Depending upon line strength and available exposure time, it appears possible to record data out to $\approx 220\text{ Å}$; no data below 170 Å are recorded because aluminum light-blocking filters are used at the entrance aperture and at the focal plane. We note that line multiplets, such as Fe XII near 193 Å, do not smear the image, because this is a non-dispersive system.

The TXI sounding rocket program has just received approval from NASA to begin construction (May 1996). Present plans are to have the payload ready to fly by the summer of 1998. A summer launch is necessary in order to reduce absorption by the residual atmosphere even at rocket altitudes. A minimum altitude of 100 miles is necessary for the wavelengths observed in this experiment, and a line of sight to the Sun as near normal to the plane of the atmosphere as possible is required. The launch therefore takes place around local noon in White Sands, NM.

3.3. THE SOLAR RADIO TELESCOPE

Of course, it is not only in the area of space-based instrumentation that solutions to the present set of problems in solar physics may be sought. In this section we describe a representative ground-based instrument, designed to map the magnetic field structure and topology in the corona.

A proposal for a dedicated Solar Radio Telescope which represents a major advance on current radio facilities is currently being explored (a report by D. Gary and T. Bastian will be available shortly). The ability to map solar magnetic fields

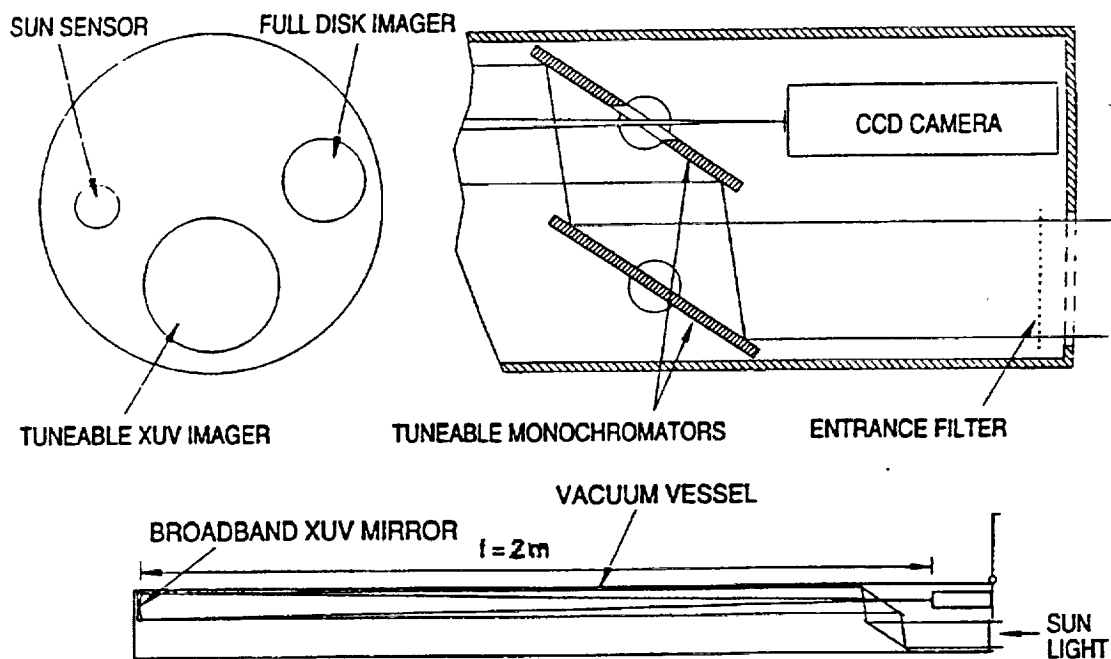


Figure 11. Schematic layout of the Tuneable XUV Imager.

Table III
Strongest lines in the TXI passband

Ion	Wavelength (\AA)	$\log T$
Fe IX	171.08	6.0
O V	172.17	5.4
O VI	172.94	5.5
	173.08	
Fe X	174.53	6.1
	177.24	
Fe XI	180.42	6.2
Si XI/Fe XII	186.88	6.2
Fe XI	188.22	6.2
Fe XXIV	192.03	7.3
Fe XII	192.40	6.2
	193.52	
	195.13	
Fe XIII	202.04	6.2
	203.82	
Fe XIV	211.32	6.3
He II	237.35	4.7

above coronal active regions is one of the major goals of this telescope. The features necessary to carry out such a goal are:

- the ability to make radio images of active regions on short time scales with high spatial resolution and high dynamic range;
- the ability to make images at many closely-spaced frequencies across a broad frequency range nearly simultaneously; and
- accurate polarimetry.

The proposed instrument which provides these features consists of an array which contains many small dishes (presently planned to be 40) with full-disk coverage, three large (~ 25 m) dishes to provide sensitivity and allow accurate calibration, and receivers which incorporate the frequency agile characteristics so successfully demonstrated by the OVRO array with a target range from 300 MHz to 30 GHz. This instrument would have 2.5 times as many baselines as the VLA, and requires a large correlator to handle them. Recent advances in broadband microwave components, large correlators and computers make such an instrument possible for a low cost. Considerable effort will also be expended on software for real-time processing of the data into a form (images and coronal field maps) suitable for immediate use by the broader solar community.

3.3.1. *Vector Magnetic Fields*

Finally, we mention the almost obvious point that vector magnetograms are crucially important in the comparison between surface fields and coronal structure/stability. Ground-based observations have progressed enormously, but there still remains the basic question: how much of the observed variability is due to atmospheric effects and how much is intrinsic to the source? This question has been answered in part by comparing observations taken simultaneously at widely-separated sites. However, the best way to answer the question and to obtain the highest quality observations, is to place a vector magnetograph in orbit.

Acknowledgements

Much of the work herein reported was supported by grants from NASA to the Smithsonian Astrophysical Observatory.

References

- Alissandrakis, C. E.: 1981, *Astron. Astrophys.* **100**, 197.
 Berger, M. A.: 1985, *Astrophys. J. Suppl.* **59**, 433.
 Billings, D. E.: 1966, *A Guide to the Solar Corona*, Academic Press, New York.
 Craig, I. J. D., McClymont, A. N., and Underwood, J. H.: 1978, *Astron. Astrophys.* **70**, 1.
 Daw, A., DeLuca, E., and Golub, L.: 1995, *Astrophys. J.* **453**, 929.
 Démoulin, P., Balala, L. G., Mandrini, C. H., Hénoux, J. C., and Rovira, M. G.: 1996, *Astron. Astrophys.*, in press.
 Golub, L., Hartquist, T. W., and Quillen, A. C.: 1989, *Solar Phys.* **122**, 245.
 Golub, L., Herant, M., Kalata, K., Lovas, S., Nystrom, G., Pardo, F., Spiller, E., and Wilczynski, J.: 1990, *Nature* **6269**, 842.

- Gómez, D. O., Martens, P. C. H., and Golub, L.: 1993, *Astrophys. J.* **405**, 767.
- Herant, M., Pardo, F., Spiller, E., and Golub, L.: 1991, *Astrophys. J.* **376**, 707.
- Heyvaerts, J. and Priest, E. R.: 1984, *Astrophys. J.* **137**, 63.
- Huber, M. C. E., Foukal, P. V., Noyes, R. W., Reeves, E. M., Schmahl, E. J., Timothy, J. G., Vernazza, J. E., and Withbroe, G. L.: 1974, *Astrophys. J.* **194**, L115.
- Linsky, J. F. and Serio, S. (eds.): 1993, *Physics of Solar and Stellar Coronae*, Kluwer Academic Publishers, Dordrecht, Holland.
- Low, B. C.: 1990, *Ann. Rev. Astron. Astrophys.* **28**, 491.
- Martens, P. C. H. and Gómez, D. O.: 1992, *Publ. Astron. Soc. Japan* **44**, L187.
- Metcalf, T. R., Canfield, R. C., Hudson, H. S., Mickey, D. L., Wülser, J. P., Martens, P. C., and Tsuneta, S.: 1994, *Astrophys. J.* **428**, 860.
- Poletto, G., Vaiana, G. S., Zombeck, M. V., Krieger, A. S., and Timothy, A. F.: 1975, *Solar Phys.* **44**, 83.
- Rosner, R., Tucker, W. H., and Vaiana, G. S.: 1978, *Astrophys. J.* **220**, 643.
- Sakurai, T. and Uchida, Y.: 1977, *Solar Phys.* **52**, 397.
- Sams, B. J., III, Golub, L., and Weiss, N. O.: 1993, *Astrophys. J.* **399**, 313.
- Schmieder, B., Démoulin, P., Aulanier, G., and Golub, L.: 1996, *Astrophys. J.*, in press.
- Shibata, K. *et al.*: 1992, *Publ. Astron. Soc. Japan* **44**, L173.
- Shimizu, T., Tsuneta, S., Acton, L. W., Lemen, J. R., and Uchida, Y.: 1992, *Publ. Astron. Soc. Japan* **44**, L147.
- Tarbell, T. D., Bruner, M., Jurcevic, B., Lemen, J., Strong, K., Title, A., Wolfson, J., Golub, L., and Fisher, R.: 1994, *Proc. of the 3rd SOHO Workshop*, ESA SP-373.
- Taylor, J. B.: 1974, *Phys. Rev. Letters* **33**, 1139.
- Uchida, Y., McAllister, A., Strong, K. T., Ogawara, Y., Shimizu, T., Matsumoto, R., and Hudson, H. S.: 1992, *Publ. Astron. Soc. Japan* **44**, L155.
- Vaiana, G. S., Krieger, A. S., and Timothy, A. F.: 1973, *Solar Phys.* **32**, 81.
- Yoshida, T., Tsuneta, S., Golub, L., Strong, K., and Ogawara, Y.: 1995, *Publ. Astron. Soc. Japan* **47**, L15.

Analysis and comparison of loop structures imaged with NIXT and Yohkoh/SXT

V. Di Matteo¹, F. Reale², G. Peres², and L. Golub³

¹ Osservatorio Astronomico, Piazza del Parlamento 1, 90134 Palermo, Italy (e-mail: dimatteo@oapa.astropa.unipa.it)

² Dipartimento di Scienze Fisiche e Astronomiche, Università di Palermo, Sezione di Astronomia, Piazza del Parlamento 1, I-90134 Palermo, Italy, e-mail: reale@oapa.astropa.unipa.it, peres@oapa.astropa.unipa.it

³ Smithsonian Astrophysical Observatory, 60 Garden Street, Cambridge, MA 02138, USA, e-mail: golub@corona.harvard.edu

Received / Accepted

Abstract. We analyze and compare five coronal regions simultaneously observed by NIXT and Yohkoh/SXT on April 12, 1993. The compact loop structures (length $\sim 10^9$ cm) imaged in three regions with NIXT and with SXT have a good general morphological correspondence. A large scale ($\approx 1.7 \times 10^{10}$ cm) and an intermediate scale ($\approx 5 \times 10^9$ cm) structure observed in the NIXT image have no obvious counterpart in the SXT image. The pressure of the loop plasma detected by NIXT is derived from the brightness profile along the loops by applying a method based on loop models. The pressure of the loop plasma in the SXT band has also been derived from loop models on the basis of the temperature obtained from the standard Yohkoh data analysis. NIXT pressures are systematically lower than those found with SXT. By comparing the measured total loop luminosity to that expected on the basis of loop models, we constrain quantitatively the volume filling factor of the plasma emitting respectively in the NIXT and SXT bands. The filling factors obtained in the NIXT band for the compact and intermediate loops are very low ($10^{-3} - 10^{-2}$), but they are of the order of unity for the large structure. The low filling factors suggest a strong loop filamentation. The filling factors for the compact structures are instead of the order of unity in the SXT band. We discuss our results and propose a scenario for their interpretation.

Key words: Sun: corona – Sun: X-rays

1. Introduction

Achieving high temporal and spatial resolution in solar X-ray observations is one of the main challenges of solar coronal physics. There is evidence that the solar corona is structured down to sub-arcsec dimensions (Gomez et al. 1993). On the other hand, plasma theory applied to the corona suggests that the magnetized plasma is subject of

significant filamentation (van den Oord 1992, Litwin & Rosner 1993, Velli 1995). Such a filamentation has also been invoked as a means to generate and distribute efficiently heat released by instabilities in magnetized plasma (Parker 1988).

The SAO Normal Incidence X-ray Telescope (NIXT, Golub & Herant 1989) represents one of the fundamental steps toward obtaining the sub-arcsec spatial resolution required to observe the very small scales. For an exhaustive analysis and interpretation of the observations made by the NIXT it is important to obtain information about the physical conditions of the emitting plasma. Such a task is not straightforward with NIXT, since its single and narrow spectral band practically inhibits the application of temperature diagnostic methods, and in particular the filter ratio method used by wide band telescopes such as the Soft X-ray Telescope (SXT) on board the Yohkoh satellite.

This work is devoted to analyze and interpret the observation of selected coronal loop structures made simultaneously by NIXT and Yohkoh/SXT on April 12, 1993 (see also Yoshida et al. 1995), in order to obtain a detailed and accurate scenario taking advantage of the different insight provided by the two instruments.

Our analysis is enriched by the determination of the pressure of the plasma emitting in the NIXT band, made possible by the application of a method developed previously by Peres et al. (1994, hereafter Paper I). This method is based on extensive loop modeling and allows us to evaluate the plasma pressure directly from the analysis of the NIXT brightness distribution along the loops.

Our models show that the pressure, in a hydrostatic loop of given length, determines the temperature distribution along the loop of the confined plasma. If the plasma is observed through a narrow spectral band, such as the NIXT band, including very few spectral lines with specific formation temperatures, the brightness distribution along the loop will be strongly influenced by the plasma temperature.

On the basis of the loop emission in the NIXT pass-band, synthesized from the results of hydrostatic loop models, it has been shown in Paper I that the shape of the brightness distribution changes with pressure, yielding bright footpoints in high pressure loops and a more uniform brightness in lower pressure loops. Here we present the first quantitative application of this pressure diagnostics, which can be applied, after proper calibration, to any imaging instrument with a narrow pass-band around 10^6 K.

As an implication of the pressure determination, by comparing the observed NIXT loop total luminosity to that predicted from hydrostatic models, we are able to estimate the volume filling factor of the plasma emitting in the NIXT band and the level of filamentation in the observed loops.

In order to obtain a scenario as complete as possible we perform the same kind of analysis on Yohkoh/SXT data, for which direct temperature diagnostics are possible and thereby obtain information complementary to that of NIXT.

NIXT and Yohkoh/SXT are characterized by different optics and detectors, which result in significant differences in their response to the plasma temperature. NIXT is based on multi-layer normal-incidence mirrors which yield high reflectivity and a high spatial resolution ($1.2''$) in a narrow spectral band centered on 63.5 \AA and 1.4 \AA wide (Golub et al. 1990). This band contains the intense MgX at 63.5 \AA and Fe XVI at 63.7 \AA lines, which determine a maximum instrument sensitivity to plasma radiating between 1 and 3 MK. Yohkoh/SXT (Tsuneta et al. 1991) instead is based on grazing-incidence optics, has a lower spatial resolution ($2.5''$), a much wider spectral band, with the possibility of using various filters, and is more sensitive to higher temperatures (roughly speaking above 2.5 MK).

Given the sensitivity to plasma at different temperatures, we expect *a priori* significant differences in the detectable plasma and therefore both in the morphological appearance of the coronal structure and in the physical conditions of the detected plasma. Indeed, the sensitivity to different temperatures has been invoked by Yoshida et al. (1995) to explain the significantly different appearance of some coronal structures, different from those selected by us, detected in the two simultaneous observations made on April 12, 1993.

Our analysis of the two observations, and their combination and comparison, allow us to go beyond the simple confirmation that the two instruments look at plasmas in different thermal conditions, and provide us with a very rich scenario of the loop structuring and conditions, as we will illustrate in the following.

In section 2, we select and describe the loop structures as observed with NIXT and Yohkoh; in section 3 we analyze the NIXT data, and evaluate the plasma pressure and the volume filling factor; in section 4 we analyze the

corresponding structures in SXT images. In section 5 we discuss the results and draw our conclusions.

2. The Loop Structures

Fig. 1 and 2 show the full-sun NIXT and SXT images, respectively, taken virtually simultaneously on April 12, 1993. The NIXT data were taken between 17:17 and 17:23 UT, the SXT data between 17:11 and 17:28 UT. The NIXT image is made of 2000×2000 pixels of $1.2'' \times 1.2''$, the SXT image of 512×512 pixels of $4.91'' \times 4.91''$. The SXT image results from a combination of two single exposures of 78 and 2668 ms in the Al.1 filter (Tsuneta et al. 1991, see Sect. 4 for more details). The images have been aligned by using a fitting procedure applied to the disk limbs.

As described by Yoshida et al. (1995), many loop structures are clearly visible in the SXT image, both inside and outside the large active regions close to the disk center. There are two other active regions, one on the south-west and the other, very large, on the east limb of the disk. The loop structures are less evident in the NIXT image, although some of them are clearly visible inside and close to the active region at the center of the disk.

The loops to which we apply our pressure diagnostics have been selected from the NIXT full disk image (Fig. 1). The identification of loop structures from X-ray images is, in general, non-trivial; since the Skylab era (e.g. Vaiana 1976) it has become clear the need to identify loops with the aid of magnetograms. Therefore we have taken advantage of magnetograms to identify the loop footpoints. The magnetograms were taken by P. Hartmann of Kitt Peak Solar Observatory between 15:11 and 16:06 UT, about one hour before the X-ray images. We have corrected for the shift due to solar rotation and aligned the magnetograms to the images. We have then selected rectangular regions including single loop structures with the following two basic requirements:

1. the candidate loop structures in the NIXT image have to be isolated from other structures;
2. the extremes of the loop structures in the X-ray image must correspond to opposite polarity spots in the magnetograms.

The need for an unequivocal identification of the loop structures may impose a bias to select bright, and therefore preferentially high pressure, loops but we will show that our small sample includes pressure values spanning more than a decade, from values typical of quiet regions to those of active regions. We have selected five regions, which we will identify in the following with A, B, C, D, E in decreasing order of solar latitude, as shown Fig. 1 and, in more detail, in Fig. 3. Their characteristics, as derived from the analysis of the NIXT image, are reported in Table 1, together with relevant physical parameters derived according to the procedures illustrated in Sect. 3.

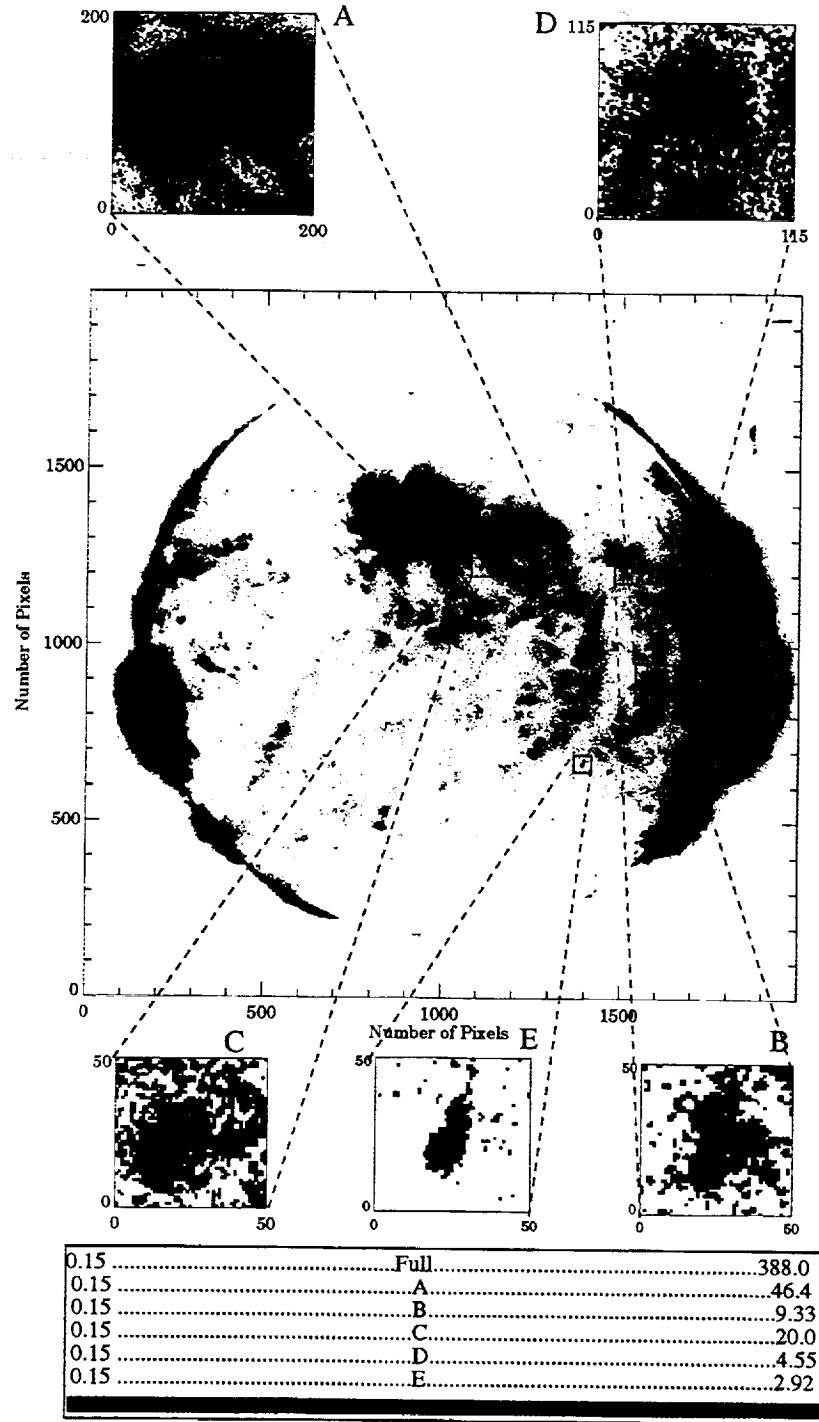


Fig. 1. NIXT solar image of April 12, 1993: the insets expand the regions where loop structures have been selected for analysis. The brightness color scales, indicated at the bottom for all panels (full disk and subregions), are logarithmic (cgs units).

Region A, slightly to the east of the central active region (Fig. 1), shows a large loop structure (the distance between the footpoints is $\approx 10^{10}$ cm) with evident footpoints, which correspond to regions of opposite polarity in

magnetograms. The loop appears to lie in a plane almost perpendicular to the line of sight, and it does not overlap with other structures, in spite of its large extension, except for a bright structure not far from the apex.

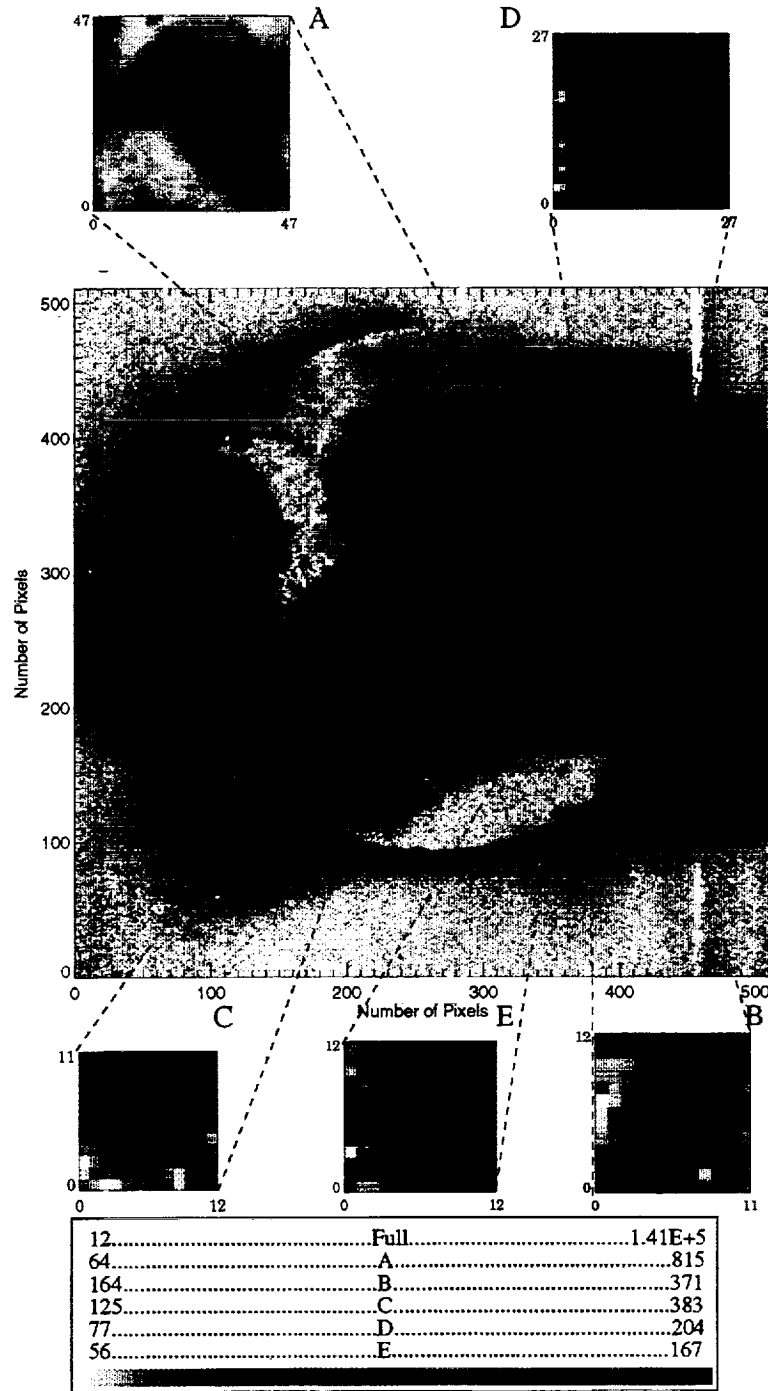


Fig. 2. Yohkoh/SXT solar image of April 12, 1993: the insets expand the same regions as the corresponding insets in Fig.1. As in Fig.1, the color scales are logarithmic (DN/s).

Regions B, C and E contain candidate isolated loops of relatively small extension ($\approx 10^9$ cm). The loops connect opposite polarities, thus suggesting that they are seen from above.

The loop structure in region D is very faint and not well defined. The results concerning this region will therefore be taken with proper care. Along this arch there are some small bright structures, which mix significantly with the loop.

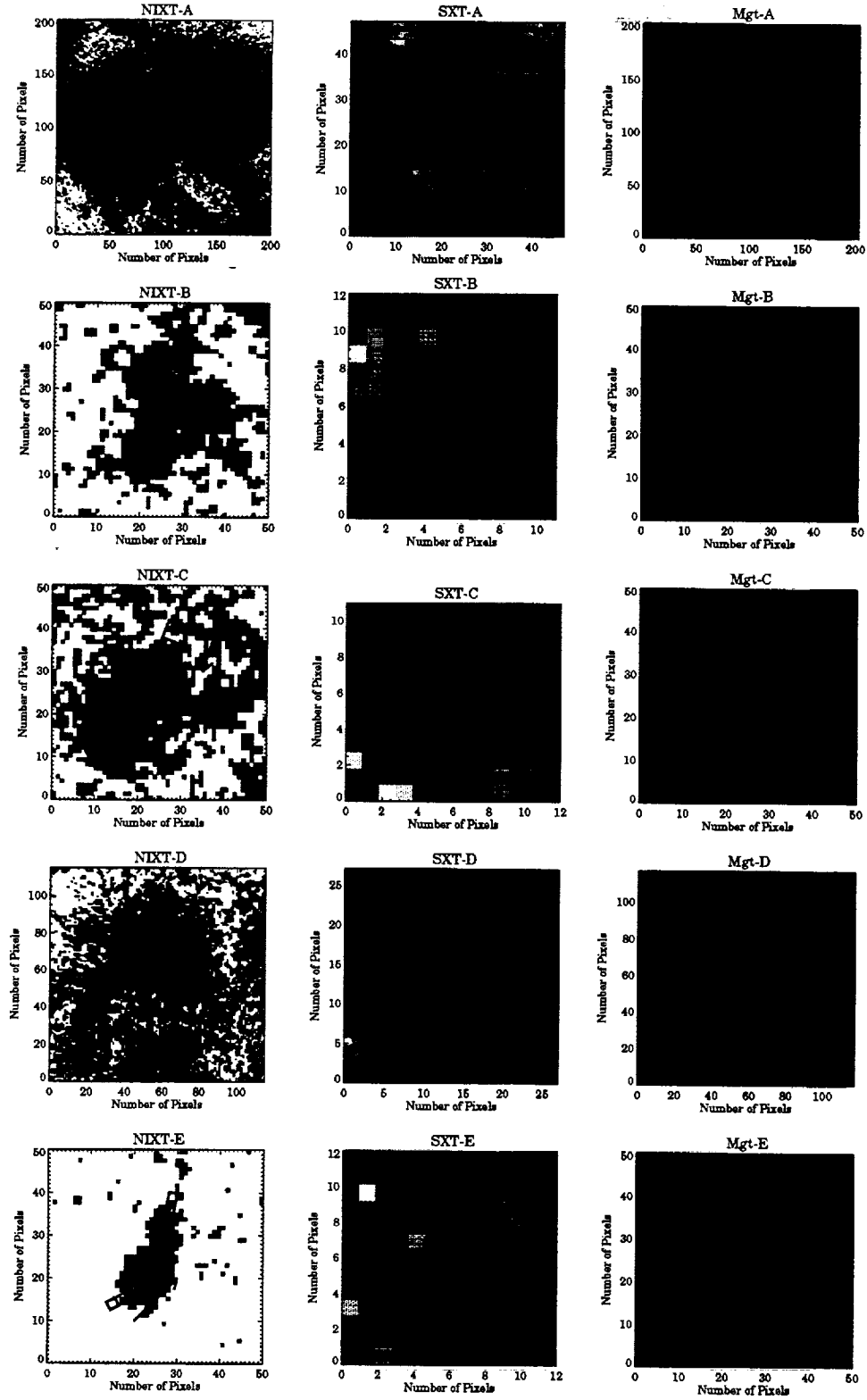


Fig. 3. Analyzed loop structures: the first and second columns show the insets of Figs. 1 (NIXT image) and 2 (SXT image) respectively, the third column the corresponding magnetograms (courtesy of NSF/Kitt Peak, from a collaboration of NSF/NOAO, NASA/GSFC and NOAA/SEL). In the NIXT frames the solid strips bound the inferred isolated loops, divided into rectangular sectors for the analysis. The corresponding strips and the appropriate division into sectors are marked also in the SXT insets. In the NIXT frames, the arrows indicate the positive direction of the NIXT brightness profiles in Fig. 5. Contour plots of NIXT brightness are shown in the magnetograms. The color scales of the magnetograms are linear (blue negative, green neutral, red positive) and range between -146 G and 146 G for regions A and C and between -73 G and 73 G for regions B, D, and E.

Table 1. Analysis of loop structures imaged with NIXT.

	A	B	C	D	E
Area	241.2" x 241.2"	61.2" x 61.2"	61.2" x 61.2"	139.2" x 139.2"	61.2" x 61.2"
latitude ^a	22.44°	13.98°	9.70°	-7.64°	-24.20°
longitude ^a	12.22°	37.32°	2.96°	47.47°	26.59°
\mathcal{D}^b (10 ⁹ cm)	10.2 ± 0.6	1.32 ± 0.06	1.22 ± 0.15	3.41 ± 0.21	1.25 ± 0.06
L^c (10 ⁹ cm)	8.5 ± 0.5	1.31 ± 0.06	1.01 ± 0.13	2.71 ± 0.17	0.99 ± 0.05
x^d (pixel)	20	2	5	7	2
y^d (pixel)	10	3	3	6	3
N^d (pixel)	13	5	3	9	3
C^e	9.5 ± 1.2	2.2 ± 0.2	3.0 ± 0.6	2.23 ± 0.09	2.9 ± 0.2
p^f (dyne/cm ²)	0.081 ^{+0.002} _{-0.007}	0.52 ^{+0.05} _{-0.03}	0.33 ^{+0.02} _{-0.03}	0.23 ^{+0.02} _{-0.01}	0.53 ^{+0.03} _{-0.07}
$\text{Log}(T_M)^f$ (°K)	6.11	6.09	5.98	6.08	6.06
$\text{Log}(ff)^f$	-0.64 ± 0.15	-2.63 ± 0.11	-2.14 ± 0.13	-2.70 ± 0.12	-2.99 ± 0.13

^a - Coordinates of the center of the selected regions;^b - Distance of the footpoints;^c - Loop half-length;^d - Width, length and total number, respectively, of the sectors in which each loop has been divided for the analysis;^e - Average luminosity contrast between the sectors at the footpoints and the apex of the loops;^f - pressure, maximum temperature (obtained from scaling laws) and volume filling factor, respectively, of the loop plasma emitting in the NIXT band.

3. The Analysis of NIXT data

3.1. The method

The approach to deriving the physical conditions inside the loops seen by NIXT, in a single narrow spectral band, is to compare the brightness distribution along the observed loop structures to that resulting from hydrostatic loop models. The SXT observations confirm that the emitting structures do not change significantly during the observation over a time scale of ~ 15 minutes, according to the general evidence that such structures live over time scales longer than the radiative and conductive cooling times (hours).

Therefore, in agreement with the hypothesis of Paper I, we consider a hydrostatic model of a coronal loop, semi-circular, of constant cross section, symmetric with respect to its apex; the equations are those of plasma hydrostatic equilibrium and of energy balance among radiative losses, thermal conduction and a phenomenological term of local heat input in the plasma. The lower boundary of the loop is set at $2 \cdot 10^4$ K. We refer to Paper I for further details.

The models are uniquely identified by p_0 , the plasma pressure at the base of the arch and by L the loop semi-length, which determine T_{max} , the maximum plasma temperature, located at the loop apex; these parameters are linked by the scaling laws of Serio et al. (1981).

Paper I shows that the brightness distribution along the loops, as observed by NIXT, depends on the loop base pressure. For high base pressure ($p \gtrsim 1$ dyne cm⁻², for loops with $L \sim 10^9$ cm) the loop brightness is high and has a sharp maximum at the loop base, whereas the brightness is much more uniform (and lower) at lower pressure. The dependence of the emission distribution on pressure is a consequence of the dependence of the maximum tem-

perature on pressure, according to the Serio et al. (1981) scaling law. This dependence of emission profile on plasma pressure occurs for any loop length considered, although the specific maximum temperature and brightness distribution depend also on the loop length.

On the basis of these results, in Paper I it is expected that footpoints are very bright immediately above the transition region in all the high pressure loops, typically found in active regions, and therefore it is possible to identify high pressure coronal regions in NIXT pictures. On the other hand, faint loop structures, if detected at all, are expected to be observed as entire loops in NIXT images, given the uniform brightness distribution predicted by the modeling.

Given the property that the profile of the brightness along the loop depends mostly on the plasma pressure, the loop plasma pressure can be determined by matching the NIXT brightness distribution, synthesized from the loop models, to the observed one. However obtaining a brightness distribution directly comparable with models is, in practice, very difficult, because the loop orientation is unknown. Furthermore the brightness profiles derived along the loops typically show fluctuations which make an accurate comparison even more difficult.

Therefore we have chosen to take the brightness contrast ($C = b_{foot}/b_{top}$) of the footpoints to the apex of the loop as indicator of the brightness distribution shape. Operatively the loops that we analyze are those for which we are able to mark an arc between two footpoints, and this is possible only as long as the footpoints are brighter than the rest of the loops. This implies that our selected loops will all have $C \gtrsim 1$, i.e. they are relatively high pressure loops. Of course, this implies a selection effect, but it is unavoidable also because low pressure loops are faint.

Even the contrast C depends moderately on the loop orientation with respect to the observer, as shown in Fig. 4, which reports the contrast C between the luminosity in the NIXT band at the base and at the apex of model loops of various lengths vs. the base pressure. The luminosity is obtained by integrating the emission per unit volume on the labeled bin size (in pixels) along the loop. Each column shows the resulting contrast for a different extreme orientation: side view and top view, respectively. The contrasts are higher for loops seen from the top, as may be expected since the footpoint luminosity includes a significant vertical section of the loop.

For a given semilength and for low contrasts, C generally increases with the pressure as expected. However, above a contrast threshold, which depends on the spatial integration step, on the loop orientation and on the loop length, the contrast has a maximum and then decreases. For such high contrasts therefore we do not have a univocal pressure diagnostics. This limit does not affect our results: as we will see in the following, we have been able to find univocal pressure values for all our selected loops. Since all selected loops are well inside the solar disk we have neglected the effect of different orientations with respect to the loop axis.

The loop models yield results per unit cross sectional area. The expected total loop luminosity is then obtained by multiplying the model brightness integrated along the loop by the loop cross-sectional area. This luminosity can be compared to the luminosity measured on the calibrated images. The ratio of the two provides a quantitative measurement of the volume fraction effectively occupied by the emitting plasma, i.e. the loop plasma filling factor in the instrument band. This ratio is expected to be always smaller than (or at most equal to) unity, i.e. the model luminosity should always be larger than (or equal to) the measured luminosity. Errors in the aspect determination and on the loop cross section however allow for ratios larger than 1.

3.2. The results

3.2.1. The pressure

In order to apply the pressure diagnostics we first evaluate the half-length L of the selected loops. Assuming semicircular loops (such an assumption is not critical), the half-length can be obtained from the distance between the footpoints d , $L = \pi d/4$. For d we have taken the linear distance between the brightest pixels at the two opposite sides of a loop. This was not possible for region D, for which, instead, we have taken the distance between the magnetic poles from the magnetograms. The main error source on d is associated with the transversal section of the loop, as determined from the analysis of the brightness distribution perpendicular to the magnetic field lines, taken close to the loop footpoints, where the signal is more intense. The

position of the loop footpoints is generally included within the transversal profiles and to be conservative we have taken half of the full width half maximum (FWHM/2) of one of the two profiles (the more well-behaved) as the inaccuracy on the position of the footpoint. The error on d then will be the root sum square of the uncertainties of the two footpoint positions, i.e. $\text{FWHM}/\sqrt{2}$. The values obtained for L are shown in Table 1, and are all between 10^9 and 10^{10} cm.

Then we extract the brightness distributions along each loop. We first mark a sequence of pixels which follow the loop structure as close as possible. The pixels are then connected by a line. In order to increase the signal to noise ratio, we consider a strip of pixels centered on this path, and divide this strip into sectors with approximately the same area (i.e. including the same number of pixels). The FWHM of the transversal brightness distribution described above is taken as the strip width x . As size of each sector along the loop we take the characteristic length in which the brightness decreases from the maximum to 1/3 of the maximum, and in such a way that: i) the number of sectors is odd, so that the central sector, usually the one containing the brightness minimum, is univocally and well identified; ii) the number of sectors is ≥ 5 , enough to obtain a proper brightness distribution. For region D, the low signal required to select sectors as large as possible: ~ 50 pixels are contained in each of the 11 sectors selected. This selection allows us also to obtain a well-defined brightness profile, as well as to avoid that the bright points are included in the region of minimum intensity.

The pixel brightness has then been averaged on each sector and the resulting brightness distributions along the paths are shown in Fig. 5.

As described in Section 3.1, the brightness contrast between the footpoints and the apex is the figure used to evaluate the pressure in the selected loops. Before computing this contrast, the background brightness is subtracted from the brightness along the loops. The background brightness for each loop has been evaluated in a small region outside of the loop, close to the loop apex, the point of minimum brightness. Its value changes from region to region, and ranges from 10% to 40% of the brightness at the loop apex. For each loop we obtain two values of the contrast, one for each footpoint (C_1 and C_2), which in general differ from each other. We have then taken the average $C = (C_1 + C_2)/2$ as the best contrast estimate and $\Delta C = |C_1 - C_2|$ as its uncertainty. We have estimated this uncertainty to be dominant with respect to others, such as fluctuations, statistical noise, and it includes that due to the chance alignment of other structures. We have verified on strips wider than 2 pixels, that halving the strip width changes the contrast values by less than 10%.

From the loop half-length L and the brightness contrast C , the pressure is evaluated with the method outlined in Sect. 3.1. In order to compare homogeneous quantities,

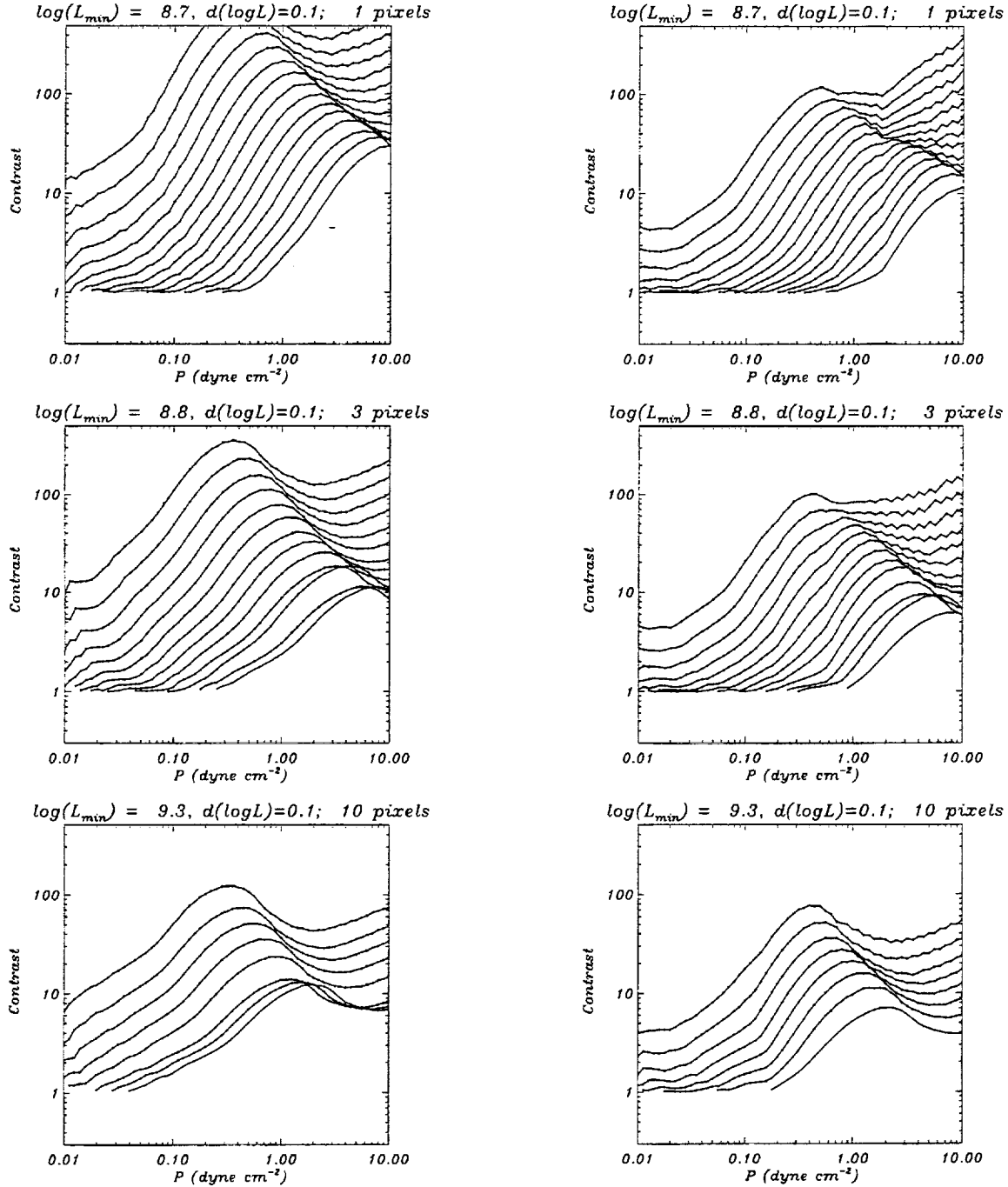


Fig. 4. Luminosity contrast of loop footpoint with respect to the loop apex in the NIXT band vs pressure, as predicted from loop model. Each solid line pertains to model loops with the same length. The lowest line is for the shortest loop (L_{\min}), higher lines are for longer and longer loops with the labeled step of increasing length. The three rows of figures are for different sizes (in pixels, in the figure labels) of the length step along the loop over which the luminosity is integrated. In the first column the contrast is computed assuming the loop as seen from above, the second as seen with a front view.

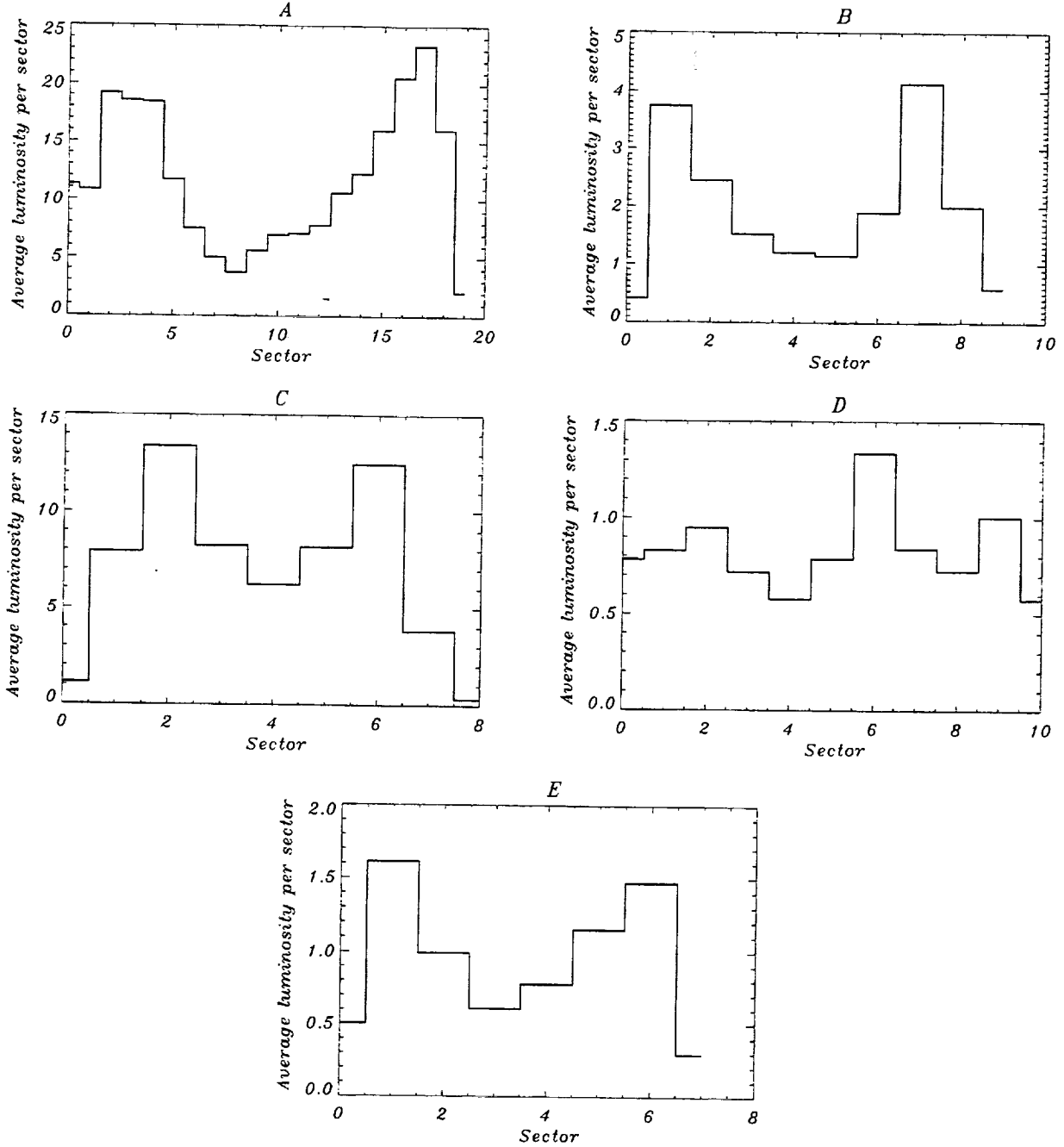


Fig. 5. Loop brightness profiles along the paths drawn in Fig.3. The brightness is averaged in the sectors marked in Fig.3.

we bin the plasma emission synthesized in the NIXT band from the models along the loop, with bin sizes of the same length as that of the loop sectors selected on the NIXT image, i.e the number of pixels y in Table 1. The resulting contrasts are shown in Table 1.

Data and models can now be compared on homogeneous ground. For a detailed comparison, we have generated a grid of loop models as fine as to minimize the uncertainty due to the discreteness of the grid. For each estimated loop length, the base pressure of the model loops range between 0.1 and 10 dyne/cm², increasing with log-

arithmetic step $\Delta \log p = 0.5$. The jump of pressure from one model to the next is $\sim 2\%$ whereas the average uncertainty from the data is $> 5\%$. From all the models we derive the brightness contrast between the base and the top sector, considering the two possible extreme loop orientations with respect to the observer, as seen from the front and from above (see Sect. 3.1). The loop morphology is taken as good evidence that loops in regions **A** and **D** are seen from the front, and therefore their contrast can be compared to the contrasts in the first column of Fig. 4, and that the others are seen from above (second column in Fig. 4).

The best value of the pressure of the observed loop with contrast $C \pm \Delta C$ is the pressure of the model whose contrast is the closest to C . The uncertainty on the pressure is determined from ΔC in the same way. The pressure values p are shown in Table 1, together with the loop maximum temperature T_M estimated from the scaling laws of Serio et al. (1981).

We have verified that the other loop orientation reduces the pressure by a factor ~ 4 for loops **A** and **D**, and increases it by a factor ~ 2 for the others. The values of the NIXT filling factor, discussed in the following, are instead much less affected by this assumption, except for that of loop **A**, which becomes larger than unity if the loop is assumed to be seen from above, clearly an unreasonable result.

In the following we summarize and discuss the results for each selected loop:

Loop **A** : The resulting relatively low pressure value is consistent with the loop being a large scale structure, with a diameter $\approx 15\%$ of the solar radius. The temperature estimated from scaling laws is close to that to which NIXT is most sensitive.

Loops **B**, **C**, **E** : due to their similarity, these compact structures can be discussed together. Their dimensions are typical of active region loops, but the pressure values are somewhat lower. Also their temperature is in the range of the instrument maximum sensitivity.

Loop **D** : This loop of intermediate size has an intermediate pressure value, and yields a temperature similar to the others.

In general we notice that the smallest selected loops tend to yield higher pressures than the largest ones. We cannot exclude a selection effect of the instrument pass-band, which tends to detect more easily structures with plasma at temperatures close to the temperature of maximum sensitivity. From the point of view of the scaling laws this is equivalent to fixing the product pL , so that smaller L implies larger p .

3.2.2. The volume filling factor

The length L and the pressure p uniquely identify a loop model among those of Serio et al. (1981), of which we have

synthesized the emission in the NIXT band. We now compare the total observed loop luminosity to that expected from the models. For a homogeneous comparison with the image calibrated brightness, we integrate the emission per unit volume derived from the model on the sector length y , multiplied by the width x , and divided by the same sector section z as the one used for the data. We find that the model brightness is systematically larger than the measured one, consistent with the expectation of plasma volume filling factors generally smaller than 100%. The ratio of the measured and expected brightnesses provides us with a quantitative estimate of the volume filling factor for loops visible in the NIXT band, shown in the last row of Table 1. The uncertainties take into account also an average data calibration error of 20%. The results are:

Loop **A** : the filling factor is relatively high, comparable to unity.

Loops **B**, **C**, **D**, **E** : the filling factor is very small, between 0.1% and 1%.

Such a wide range of filling factor values, spanning three orders of magnitude, excludes the presence of dominant calibration systematic effects on the results.

4. The Yohkoh/SXT data: morphology, pressure and filling factor

Two SXT images, close in time and made in two different filters, allow us to obtain maps of temperature and emission measure. The temperature is obtained directly from the ratio of the brightness in the two different filters. The emission measure is obtained from the ratio:

$$EM = \frac{B_k}{G_k(T)} \quad (1)$$

where B_k and G_k are the pixel luminosity and the expected luminosity per unit emission measure in the k -th filter.

The SXT data are taken in the Al.1 and AlMg filters (Tsuneta et al. 1991). We have combined couples of short and long exposure images (78 and 2668 ms in the Al.1 filter, 168 and 5338 ms in the AlMg filters) to obtain a higher dynamic range. In order to identify the same regions already selected in the NIXT image, the SXT and NIXT images have been co-aligned in the same way as we did with the magnetograms. In Figs. 2 and 3 we show these regions as observed with the SXT. Region **A** contains a larger and more complex structure than that detected by NIXT, presumably a bundle of adjacent loops, whereas NIXT seems to detect a single structure. The same path as marked on the NIXT image does not seem to mark so clearly a single loop as, instead, it does on the NIXT image. Regions **B**, **C**, and **E** are characterized by smaller bright structures, whose size is of the order of one pixel. Region **D** does not show any clearly identifiable structure on the SXT images.

The same five paths as in the NIXT image have been marked on the SXT images. We have applied our analysis on all five regions, even if for regions **A** and **D** there is no clear correspondence with loop-like structures. We have then considered strips with the same width as for NIXT images. This has been possible only for regions **A** and **D**, because the SXT pixel is 4 times larger than the NIXT pixel; for the other smaller loops we have considered a minimal strip width of 2 pixels. The strips of loops **A** and **D** has also been divided into sectors, so as to have an idea of the temperature and emission measure distribution within the loop. A single sector has been instead considered for the other loops. The detected emission has been integrated in each sector.

The resulting temperature and emission measure distributions for regions **A** and **D** are practically uniform along the selected paths within the uncertainties. On the other hand, since the paths traced to follow isolated loops on the NIXT image do not mark clearly loop structures on the SXT images, we do not expect to obtain any well-defined trend, comparable to those typical from loop models.

In order to evaluate the loop pressure from the SXT data, we assume the temperature averaged on the marked strips, T_{eff} as the loop average temperature (of the plasma emitting in the SXT band). We then consider the same grid of model loops as those used for the NIXT analysis (Sect.3) and compute their average temperature T_{mod} from the ratio of the total loop emissions synthesized in the two selected SXT filters.

Then we take as loop pressure is the base pressure of the loop model which yields $T_{mod} \approx T_{eff}$. From the ratio of the total detected loop emission to the total model emission (in one filter) multiplied by a cross-section diameter, we then derive the volume filling factor of the plasma emitting in the SXT band. The cross-section diameter has been determined as equal to the SXT FWHM at one of the footpoints, as done in the analysis of NIXT data, for the loops well-defined in SXT (**B**, **C**, **E**), and directly as equal to diameter as determined in the NIXT analysis for loops **A** and **D**. It is worth noting that the average temperature considered here is not the same as the temperature at the loop apex, the same used in the scaling laws for hydrostatic loops, but instead it is systematically lower, being an average including plasma at lower temperatures.

Table 2 shows the temperature, the emission measure per pixel, the cross-section diameter (in pixels), the loop pressure and the filling factor as derived from the method above.

As is clear from Table 2, all the pressure values derived from SXT are systematically higher (a factor 3 to 9) than those derived from NIXT. This is essentially due to the different passbands of the two instruments which select plasma at different temperatures (and therefore pressure). Even for the large region **A** the pressure value is more similar to those of active region loops. As occurred for

NIXT, the compact loops have higher pressure, typical of core active regions. The filling factors are all considerably higher than those obtained from NIXT. The values for the compact structures **B**, **C**, **E** are comprised in the range 0.1–1. Such values, not far from unity, indicate loops filled up with plasma emitting in the SXT band. Indeed, the real filling factor may be closer to unity than the obtained one, because the relatively limited resolution of the SXT image forces us probably, especially for small loops, to consider volumes outside the loop.

The value for region **D** is compatible with unity. Since this structure is not well-defined in the SXT image, we will not discuss it any further. Instead the very high value obtained for region **A** deserves some comments. As discussed previously, the boundaries which clearly identify a single loop structure on the NIXT image do not identify it as clearly on the SXT image. In the SXT image the region appears relatively less bright than the immediately surrounding region. At a first glance, one may think that the different pass-bands make the loop footpoints appear brighter in the NIXT band and the apex in the SXT band. If this were the case, we would still have obtained a realistic value of the filling factor. Such a high value instead indicates that *SXT is detecting a structure or structures different and distinct from that visible in the NIXT image and falling in the same field of view*. In fact, it is possible to obtain filling factor values comparable to, or smaller than, unity only if we consider a loop or bundle of loops considerably smaller/shorter than that identified in the NIXT image (as shown in Fig.2). These loops therefore are not the same loops as the NIXT loop.

An alternative way to evaluate the loop plasma pressure is to derive the density from the emission measure as in Eq. (1), by making an assumption on the emitting volume V :

$$n = \sqrt{EM/V} \quad p = 2k_B n T \quad (2)$$

where fully ionized gas has been assumed.

We can estimate the relevant volume by considering the loops as enclosed in the areas marked in Fig.3. We can then evaluate the cross-sectional area for two extreme values of loop depth along the line of sight: a) the unit depth (1 pixel = 4.9"), which corresponds to a minimal volume and therefore will yield an upper limit on pressure; b) the depth for a toroidal loop, with circular cross section with diameter equal to the strip width; in this case the "effective" depth, i.e. taking into account that it varies across the loop, is $\sqrt{\pi/4}$ of the cross diameter, and it should yield a maximum volume and therefore a lower limit on pressure.

We have verified that the pressure values derived from the EM with the above assumptions on the volume invariably lead to unreasonably high SXT filling factors i.e. much larger than one, for all our selected loops. Indeed this approach is not self-consistent since the assumptions on volume do not take into account the loop filamentation.

Table 2. Loops as imaged by Yohkoh/SXT

	$\text{Log}_{10}(T_{eff}^a)$ K	$\text{Log}_{10}(EM_{pixel}^b)$ cm^{-3}	d^c	p^d dyne/cm^2	ff^e
A ^f	6.243 ± 0.005	44.69 ± 0.02	5	$0.39^{+0.05}_{-0.04}$	$(7.8^{+3.5}_{-2.4})^g$
B	6.28 ± 0.05	44.3 ± 0.3	2	$3.5^{+2.1}_{-1.3}$	$0.1^{+0.3}_{-0.08}$
C	6.24 ± 0.03	44.5 ± 0.2	2	$2.8^{+1.2}_{-0.8}$	$0.4^{+0.6}_{-0.2}$
D ^f	6.19 ± 0.02	44.48 ± 0.07	3	$0.6^{+0.2}_{-0.1}$	$(1.4^{+1.3}_{-0.7})^g$
E	6.18 ± 0.06	44.4 ± 0.2	3	$1.6^{+1.2}_{-0.7}$	$0.3^{+1.1}_{-0.3}$

^a - Loop average temperature^b - Average emission measure per pixel^c - Loop cross-section diameter (in pixels)^d - Pressure obtained from SXT data on the basis of loop models^e - Volume filling factor of the loop plasma observed in the SXT band^f - The analysis has been carried out (on the same strip as marked in the NIXT image) even if the loop is not clearly identified in the SXT image^g - Not a proper plasma loop filling factor.

5. Discussion

This work studies coronal loops by taking advantage of the complementary information provided by NIXT and Yohkoh/SXT, which observed the solar corona simultaneously. NIXT works in a softer and narrower spectral band, and its spatial resolution (1.2" pixel size) is four times higher than the other instrument, while Yohkoh/SXT allows direct temperature diagnostics by using different filters. In this work, for the first time, we have applied a diagnostic method (Paper I) which allows us to evaluate the plasma pressure inside loops observed with NIXT.

The analysis described above is based on the assumption that hydrostatic loop models provide a good description of loop plasma conditions, a well-established fact for most loops (e.g. Rosner et al. 1978). The presence of moderate subsonic siphon flows driven by pressure differences between the loop footpoints should not much affect our results, because the overall physical characteristics would not change much (Orlando et al. 1995). Shocking siphon flows instead should make loops appear highly asymmetric, an effect that is not observed on our selected loops. Finally although the exact values are, to some extent, subject to improvement, their orders of magnitude are unequivocal and represent a significant result.

Since the two instruments are sensitive to plasma at different coronal temperatures, NIXT mostly around 1 MK, SXT mostly higher than 2 MK, in general we do not expect an exact correspondence between the morphology of loops detected by the two instruments. In fact, although there is a good correspondence between the location of all the selected structures observed by the two telescopes, their morphology appears clearly different. A close inspection of loop structure A shows that the path chosen along the loop in the NIXT image corresponds to a relatively "dark" structure related to the surrounding loops in the SXT images. A more detailed analysis, which includes the pressure and filling factor evaluations in both instrument bands, seems to indicate that the two instru-

ments are looking at distinct loop structures with different lengths, falling in the same field of view. In other words the low pressure derived from NIXT data would be confined in a loop not visible by the SXT, which, instead, detects the emission from co-existing higher pressure and more compact structures.

The pressure values obtained from SXT data are systematically higher than those obtained from NIXT. This result can probably be ascribed to the different spectral bands: the SXT is sensitive to hotter plasma, which is in general also at higher pressure for the same loop length. This indicates that plasmas at different temperature and pressure may coexist in the same loop structures, or, at most, in neighboring loops. Notice that our analysis shows that density values inferred from the emission measure as in Eq. (2) can be wrong and can lead to unrealistic values of pressure and filling factor.

The same detailed comparison cannot be made for the smaller loops B, C and E because of the limited resolution of the SXT. The morphology of such more compact regions appears quite similar in the SXT and NIXT images. The brightest parts detected by SXT are located close to the center of the NIXT-imaged structures and seem to coincide with the apex of the loops. For the small loops, it appears as if the combination of SXT and NIXT images would show the entire loop structure, NIXT being more sensitive to the footpoints and SXT to the apex. However, the relatively low resolution of the SXT does not allow us to put a tighter constraint on this aspect, and we cannot exclude, for instance, that the two instruments observe two adjacent loops at different pressure (SXT observing a loop at higher pressure).

We could not identify a clear counterpart of the structure D on the SXT images, probably because it is a relatively low pressure loop located in a region with other complex and relatively bright structures.

These results allow us to derive a more complete scenario than previously obtained, for instance, by Yoshida et

al. (1995). In summary, smaller and higher pressure structure are those showing the better morphological agreement between NIXT and SXT. In contrast, large structures (A and D) appear different to the two instruments both in morphology and in plasma parameters. In particular, the large loop A, clearly visible in the NIXT image, is not visible in the SXT band.

The filling factor in region A, as observed by NIXT, is large and close to 1; for the smaller structures of regions B, C and E, for which a comparison between NIXT and SXT results is sound, we find a large filling factor in Yohkoh-imaged loops and a small one in NIXT-imaged ones.

All these results may be interpreted in the light of the following scenario, known since Skylab observations: coronal loops evolve from small, hot and compact structures to progressively large, cool and extended structures. Our results add the information that smaller loops are also completely filled with high temperature plasma, detectable almost only by SXT. As they get cooler, more and more plasma filaments become visible by NIXT, although coexisting with many other hot and dense filaments. Later in the cooling, most of the loop would contain relatively cooler plasma, i.e. visible with NIXT only, and with a high filling factor. The fact that this occurs just for the large loop A is consistent with the general trend of the gradual expansion of small loops to large loops.

In this scenario, the large loop observed by NIXT in region A would be a relatively evolved and cool structure, invisible to the SXT (which instead detects under/overlying hotter structures); the more compact loops in B, C and E, would instead be hotter and with a small number of filaments visible by NIXT; region D would be in an intermediate stage between the two extremes.

We note that the low filling factors obtained for the compact loops ($1/100 - 1/1000$) strongly suggest that there is a very fine filamentation of magnetized loops within loops and provide a quantitative estimate of its value. This work therefore contributes quantitatively to the comprehension of the filamentary structure of coronal magnetic loops. Also our findings suggest that the plasma does not cool down uniformly in the loop, and that a progressively higher number of filaments get cooler, and thus become gradually visible by NIXT. This hypothesis needs further checks and verification which will surely come from forth-coming high resolution observation.

Acknowledgements. VDM, FR and GP acknowledge partial support from Ministero dell'Università e della Ricerca Scientifica e Tecnologica, Agenzia Spaziale Italiana. LG acknowledges support from NASA grant NAGW-4081.

References

- Golub L., Herant M., 1989, Proc. Spie, 1160, 629.
- Golub L., Herant M., Kalata K., et al., 1990, Nature, 344, 842.
- Gomez D. O., Martens P. C. H., Golub L., 1993, ApJ, 405, 767.
- Litwin C., Rosner R. 1993, ApJ, 412, 375.
- Orlando S., Peres G., Serio S., 1995, A&A, 294, 861.
- Parker E. N., 1988 ApJ 330 474.
- Peres G., Reale F., Golub L., 1994, ApJ, 422, 412 (Paper I).
- Rosner R., Tucker W., Vaiana G., 1978, ApJ, 220, 643.
- Serio S., Peres G., Vaiana G.S., Golub L., Rosner R., 1981, ApJ, 243, 288.
- Tsuneta S., Acton L., Bruner M., et al., 1991, Sol.Phys., 136, 37.
- van den Oord G.H.J., 1992, in Solar Physics and Astrophysics at Interferometric Resolution, L. Damè & T-D. Guyenne eds., ESA SP-344, p.97
- Vaiana G. S., 1976, Phil. Trans. R. Soc. Lond., A.281, 365.
- Velli M., 1995, in Solar Wind 8 Conference, 28.
- Yoshida T., Tsuneta S., Golub L., Strong L., Ogawara Y., 1995, P.A.S.J., 47, L15.

